Multi-material and strength-oriented microstructural topology optimization applied to discrete phase and functionally graded materials

Submitted to Structural and Multidisciplinary Optimization

Fábio M. Conde [1,2*], Pedro G. Coelho[1,2], José M. Guedes[2]

[1] UNIDEMI, Faculty of Science and Technology
Universidade Nova de Lisboa
FCT, 2829-516 Caparica, Portugal
{f.conde@campus.fct.unl.pt; pgc@fct.unl.pt}

[2] IDMEC, Instituto Superior Técnico
Universidade de Lisboa
Av. Rovisco Pais 1, 1049-001 Lisboa, Portugal
{jmguedes@tecnico.ulisboa.pt}

Abstract

Structural optimization plays an important role in lightweight construction and stresses need to be controlled to avoid material failure. The multi-material design setting offers additional design freedom which can lead to structures with improved strength and stiffness properties compared to the single-material case.

The present work addresses topology optimization of a periodic composite material unit-cell, with properties predicted by homogenization, using strength and stiffness design criteria, under bulk and mixed loading cases. Plane stress and linear behaviour are assumed. The compliance minimization with mass constraint problem is revisited here, but the paper focus is on multi-material stress-based topology optimization. Specifically, the maximal von Mises stress is minimized in the unit-cell where two solids are mixed amidst void. Depending on the material interpolation law settings, two design solutions are investigated. On one hand, the two solids coexist being bonded together across sharp interfaces. On the other hand, a functionally graded material is obtained as an extensive smooth variation of material properties on account of varying composition's volume fractions of both solids throughout the design domain. A parallel MMA version is proposed to efficiently deal with several design constraints.

The compliance-based optimization results show that multi-material microstructures can be stiffer compared to single-material ones for the same mass requirement. Regarding the stress-based problem, lower stress peaks are obtained in bi-material design solutions and, specially, in the case of graded material solutions. The latter approximates a fully stressed design which excels in stress mitigation. Therefore, the multi-material setting impacts favourably on structural performance, in both stiffness and strength-oriented designs.

Keywords: Multi-material; Stress; Topology Optimization; FGM; Homogenization; Parallel MMA

Acknowledgements

Authors acknowledge Fundação para a Ciência e a Tecnologia (FCT – MCTES) for its financial support through the projects UIDB/00667/2020 (UNIDEMI) and UIDB/50022/2020 (IDMEC/LAETA) and PhD scholarship SFRH/BD/136744/2018. Authors wish also to thank Professor Krister Svanberg (Royal Institute of Technology, Stockholm, Sweden) for the MMA optimization code.

1. Introduction

Topology Optimization (TO) finds the best distribution of material within a design space, for a given set of boundary conditions. It can be applied to discrete or continuous type design domains (Bendsøe and Sigmund 2004). The pioneer work of Bendsøe and Kikuchi (1988), where the homogenization method is presented, is followed up by other relevant TO methods such as SIMP (Bendsøe 1989), Level-Set (Wang et al. 2003), Topological Derivative (Sokolowski and Zochowski 1999) and Phase Field (Bourdin and Chambolle 2003).

The Single-Material Topology Optimization (SMTO) has been extensively studied over the past decades. Regarding the Multi-Material Topology Optimization (MMTO), there is not that much work especially in microstructural design. MMTO is a current research topic also boosted by rapid developments in Multi-Material Additive Manufacturing (MMAM), see e.g., Liu et al. (2018). It has been shown that multi-material design solutions, compared to single material, can lead to better compliance and stress levels, see e.g., Li and Kim (2018) and Coelho et al. (2021).

The classical SIMP method, so widely used in favouring "black-white" designs, can be straightforwardly extended to interpolate more than two phases, so-called Recursive SIMP, see Bendsøe and Sigmund (1999). The SIMP-based interpolation has been claimed unsuitable when applied to more than three solid phases (Stegmann and Lund 2005). It increases the computational cost rapidly, and the non-linearity of the interpolation function makes it more difficult to escape from local minima. In the present framework SIMP is applied to two solid phases. Another interpolation scheme is the Discrete Material Optimization (DMO), originally proposed to optimize the fibre orientations or materials choice in laminates (Stegmann and Lund 2005). The DMO differs from SIMP in the way that each material has its own density variable, which simplify the weight functions in the interpolation law. However, to avoid properties extrapolation, additional pointwise constraints are introduced, i.e., at each design point the sum of densities must be lower than or equal to unity, which increases the computational cost (Hvejsel and Lund 2011; Hvejsel et al. 2011). Adding more material phases means increasing likewise the number of density variables in SIMP and DMO schemes. Hence, breakthroughs on interpolation schemes, to reduce the computational cost, have been proposed, such as: Shape Function with Penalization, SFP (Bruyneel 2011 and James 2018), Peak Function (Yin and Ananthasuresh 2001) and ordered SIMP (Zuo and Saitou 2017). Besides these schemes for density-based MMTO problems, there are also other ones to solve multi-material problems using the level-set (Wang and Wang 2004; Guo et al. 2014), phase field methods (Tavakoli and Mohseni 2014; Zhou and Wang 2007), and binary-based design variables (Sivapuram et al. 2021). Sigmund and Maute (2013) discuss also different TO approaches.

In the literature, the common MMTO formulation is compliance minimization subject to volume fraction constraints on each phase. The introduction of the mass constraint in the multi-material problem has also been addressed, see e.g., Hvejsel et al. (2011); Sanders et al. (2018); Woischwill and Kim (2018); Kennedy and Chin (2019). The presence of each material phase, from a given predefined set of materials, is not enforced when a unique total mass constraint is used which may lead to interesting (non-trivial) material combinations. Besides the mass constraint, Zuo and Saitou (2017) also consider the material cost constraint, which is somehow equivalent to include volume constraints. Some authors also claim that having mass as the objective is preferable in engineering practice, although an upper bound on the compliance constraint may not be apparent (Jung et al. 2020; Li D. and Kim 2018; Long et al. 2018).

This work addresses SIMP-based MMTO in microstructural design as a follow up to the author's previous work (Coelho et al. 2021). Now one introduces an additional density design

variable and adapted formulations paving the way to stress mitigation on account of better exploring different aspects of the multi-material setting. Firstly, the compliance minimization problem under mass and/or volume constraints is revisited. The designs obtained are firstly compared to the well-known single-material Vigdergauz microstructures (Vigdergauz 2001, 2002), for plane stress conditions with macroscopic applied stresses of same sign and magnitude (bulk-type load). The Vigdergauz solutions satisfy the Equi-Stress Principle (ESP, Cherepanov 1974) which means that the hoop stresses σ_t, along the hole free-traction boundary Γ, are constant and with magnitude $\sigma_{t|\Gamma} = \mathrm{tr}\langle\boldsymbol{\sigma}\rangle/V$, where $\boldsymbol{\sigma}$ is the average applied stress tensor and V is the material volume fraction. The ESP identifies the optimal hole shape that minimizes both compliance and stress concentration. Vigdergauz (2016) also studies (analytically) a multiphase nested inclusion in a periodic cell. Inspired by that, one here aims to show that multi-material designs can outperform single material ones regarding stiffness and, mainly, stress distributions. In many applications it is of central importance to control stress concentrations inside composite structural components. Regions highly stressed are most likely to fail first during service. This motivates pursuing here strength-oriented MMTO. Pointwise control of von Mises stresses can be done either imposing the yielding stress of each interpolated material or, alternatively, minimizing the maximal von Mises stress. The former approach is more suitable when one wants to assure that the failure stress is not exceeded in any of the design materials. On the other hand, the latter is more suitable to approximate a Fully Stressed Design (FSD), ideally meaning that every material point of the structure is equally stressed, which is actually aimed in the present work.

It is worth mentioning that the microstructural stress shape optimization problem has been conveniently addressed in the literature, see e.g., Noël et al. (2017), Picelli et al. (2020), and Coelho et al. (2021). As regards dealing with stresses in TO, that is particularly challenging mainly due to: the stress function non-linearity; the singularity phenomenon; the local nature of stresses. These issues have been conveniently tackled by the TO community mainly focusing on macro-structural design, see e.g., Deaton and Grandhi (2014), while the microstructural design has been treated to a much lesser extent (Coelho et al. 2021, 2019; Collet et al. 2018). The aforementioned issues in the multi-material setting represent an increased level of complexity. Quite a few contributions on strength-oriented MMTO are found in the literature so far, either on macrostructure (see, e.g. Ramani 2011; Kennedy 2016; Zhao et al. 2021a) or microstructure design (see, e.g. Coelho et al. 2021; Alacoque et al. 2021). In Coelho et al. (2021), the authors carry out a more-like free-material optimization, where an optimal Young's modulus distribution is obtained in the unit-cell (UC) on account of setting SIMP for a linear interpolation. This renders a continuous gradation of material properties over the UC domain, in analogy with a Functionally Graded Material (FGM). This gradient-type material (GM) obtained via TO, so-called GMTO in Coelho et al. (2021), is not to be confused with what a FGM truly is, i.e., a mixture of two different homogeneous materials. It is known that properties of such mixtures do not linearly correlate with volume fractions of constituents (Ituarte et al. 2019; Xia and Wang 2008; Conlan-Smith and James 2019). This last aspect is now considered by the authors in this paper.

Although the single-material Vigdergauz microstructures, under bulk load, are equally optimal for both stiffness and strength, a stress concentration factor arises at the hole free-traction boundary. This can be reduced on account of introducing a softer homogeneous layer (ring) around the hole (Coelho et al. 2021; Vigdergauz 1993). In the present work this is done through bi-material TO. However, the resulting sharp interfaces between the two homogeneous solid phases lead to interfacial mismatch-induced stresses jeopardizing resistance to delamination or fatigue. An improved design solution involves a continuous gradation of material properties in the vicinity of the interface region (transition zone) between discrete materials. This localized

FGM design solution can be extended to the full design domain to completely explore its stress mitigation potential. This computational design approach is pursued in the present work while the fabrication of such advanced composite (FGM) constitutes another challenging work yet to be met by the research community (Ituarte et al. 2019).

In a nutshell, two different microstructural MMTO problems are addressed here. Firstly, a compliance-based MMTO problem with mass and/or volume constraints is solved to show better performance compared to the single material case. Secondly, a stress-based MMTO is performed such that the maximal von Mises stress is minimized under compliance and volume constraints. Discrete phase and functionally graded materials are obtained showing successive benefits in stress mitigation. In particular, the FGM designs found here through the solution of the FGMTO problem are a promising extension of the GMTO problem previously addressed by the authors in Coelho et al. (2021).

From a computational cost viewpoint, performing the strength-oriented MMTO has two main bottlenecks: the stress sensitivity analysis and the optimizer runtime. This is especially critical in the mixed loading cases, also addressed here, since no symmetry advantages exist which demands a parametrization of the full UC domain. Therefore, on one hand, the sensitivities obtained here through the adjoint method are speeded up by parallel computing. On the other hand, the Method of Moving Asymptotes (MMA, Svanberg 1987), the optimizer chosen here, is adapted for a parallel version proposed by the authors to specifically speedup runtime when many constraints (say thousands of stress constraints) are considered.

This paper is outlined as follows. Section 2 presents the homogenization-based material model and details the multi-material interpolation schemes used. Section 3 focuses on the TO problem, i.e., the proposed formulations, the sensitivity analysis, and the parallelization issues. Stiffness and strength-oriented microstructural optimal designs are presented in Section 4. Finally, main conclusions are presented in Section 5.

2. Material model

It is considered the in-plane repetition of a UC, defined in the square domain Y with feature size d, representing the smallest periodic heterogeneity of the material domain Ω of size D, see Fig. 1. A plane stress field $\langle\sigma_{ij}\rangle$ is remotely applied to Ω. Separation of scales is assumed, i.e., d is much smaller than D. Periodic displacement-based boundary conditions are applied to Y. The behavior of the periodic material is extracted from the UC analysis through asymptotic homogenization (Guedes and Kikuchi 1990), as detailed in Section 2.1. Section 2.2 details the density-based material interpolation law used to interpolate among void (blue), stiffer solid $\mathbf{E}_1$ (red) and weaker solid $\mathbf{E}_2$ (green), as illustrated in Fig. 1.

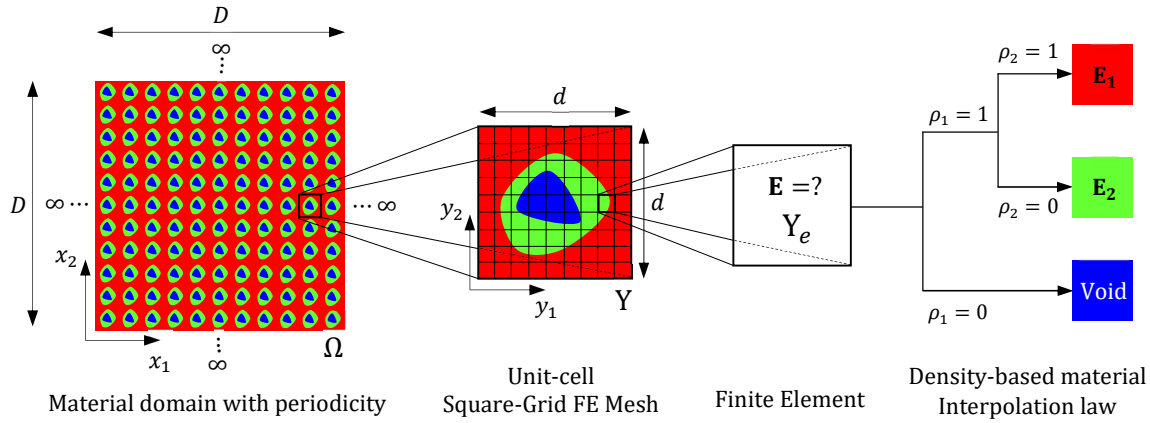

Fig. 1 Material model considering a porous composite with periodic multi-material microstructure

2.1. Homogenization method

The overall idea of the homogenization method is to replace a heterogeneous medium by a homogeneous one with equivalent properties. The equivalent or homogenized stiffness tensor $\mathbf{E}^{\mathrm{H}}$ depends on the base material stiffness tensor $\mathbf{E}$ and micro-displacements $\boldsymbol{\chi}$, by (see Guedes and Kikuchi 1990):

$$E^{\mathrm{H}}_{ijkl} = \frac{1}{|\mathrm{Y}|}\int_{\mathrm{Y}} E_{pqrs}\left(\delta_{rk}\delta_{sl} - \frac{\partial \chi^{kl}_r}{\partial y_s}\right)\left(\delta_{pi}\delta_{qj} - \frac{\partial \chi^{ij}_p}{\partial y_q}\right)\,\mathrm{dY} \tag{1}$$

where $|\mathrm{Y}|$ is the UC volume (area in 2D), and $|\mathrm{Y}| = 1$ is assumed, $\mathbf{y}$ is the position vector defined in Y and $\boldsymbol{\delta}$ is the Kronecker delta. The base material stiffness tensor $\mathbf{E}$ at a given point in the microstructure depends on the design variables (densities) as explained later in Section 2.2. The micro-displacements $\boldsymbol{\chi}$ are the solution of (2) defined in Y, comprised by a set of three equilibrium equations (in 2D):

$$\int_{\mathrm{Y}} E_{ijrs}\frac{\partial \chi^{kl}_r}{\partial y_s}\frac{\partial v_i}{\partial y_j}\,\mathrm{dY} = \int_{\mathrm{Y}} E_{ijkl}\frac{\partial v_i}{\partial y_j}\,\mathrm{dY}, \quad \forall\, \mathbf{v} \in \mathrm{Y}-\text{periodic} \tag{2}$$

where $\mathbf{v}$ are the virtual displacements, considering the weak form of the FE formulation. The periodic boundary conditions are imposed on Y by setting the same micro-displacements $\boldsymbol{\chi}$ in opposite (corresponding) nodes on the UC boundaries.

The stresses $\boldsymbol{\sigma}$ in the microstructure are computed in the following way,

$$\sigma_{ij} = E_{ijrs}\left(\delta_{rk}\delta_{sl} - \frac{\partial \chi^{kl}_r}{\partial y_s}\right)\langle \varepsilon_{rs}\rangle \tag{3}$$

where $\langle\boldsymbol{\varepsilon}\rangle$ is the macroscopic average applied strain tensor, which is related to the macroscopic average applied stress tensor $\langle\boldsymbol{\sigma}\rangle$ through,

$$\langle \varepsilon_{rs}\rangle = C^{H}_{rspq}\langle \sigma_{pq}\rangle \tag{4}$$

where $\mathbf{C}^{\mathrm{H}}$ is the homogenized compliance tensor, computed as the inverse of the homogenized stiffness tensor $\mathbf{E}^{\mathrm{H}}$ knowing that,

$$E^{\mathrm{H}}_{ijmn}C^{\mathrm{H}}_{mnkl} = \frac{1}{2}\left(\delta_{ik}\delta_{jl} + \delta_{il}\delta_{jk}\right) \tag{5}$$

The equations (1-3) are solved numerically by the FE method. The domain Y is discretized by a square-grid FE mesh, as illustrated in Fig. 1, having the element e area $|\mathrm{Y}_e|$. The von Mises stress σ_e^{VM}, in each Y_e, considers the volume average of the values computed at each Gauss point of the FE, i.e.,

$$\sigma_e^{VM} = \frac{\int_{\mathrm{Y}_e} \sqrt{\frac{1}{2}[(\sigma_{11}^e - \sigma_{22}^e)^2 + (\sigma_{11}^e)^2 + (\sigma_{22}^e)^2] + 3(\sigma_{12}^e)^2}\, \mathrm{dY_e}}{|\mathrm{Y}_e|} \tag{6}$$

The homogenized stiffness tensor $\mathbf{E}^{\mathrm{H}}$ in (1) and the micro-displacements $\boldsymbol{\chi}$ in (2) are obtained through the FE implementation `PREMAT`, and then the postprocessor `POSTMAT` is used to obtain the micro-stresses $\boldsymbol{\sigma}$ in (3) and the von Mises stresses σ_e^{VM} in (6), see Guedes and Kikuchi (1990).

2.2. Multi-material interpolation scheme

Multi-material design solutions with up to three phases (two solids and void) as well as FGM solutions are sought in the present work. To solve the density-based MMTO problem considering this number of discrete phases, both SIMP and DMO interpolation schemes can be used. However, the SIMP is chosen here as its application is straightforward to either MMTO or FGMTO problems. As explained below, SIMP adequately models the rule of mixtures in FGMTO. Therefore, the SIMP-based multi-material interpolation law (Power-law), found in Bendsøe and Sigmund (1999), is used here, i.e.,

$$\mathbf{E} = (\rho_1)^{p_1}[(\rho_2)^{p_2}\mathbf{E}_1 + (1 - (\rho_2)^{p_2})\mathbf{E}_2] \tag{7}$$

where $\rho_1, \rho_2 \in [\rho_{min}, 1]$ are the so-called artificial densities, $\mathbf{E}_1$ and $\mathbf{E}_2$ are the stiffness tensors of the solid phases (with $\mathbf{E}_1 > \mathbf{E}_2$) , p_1 and p_2 are the penalization exponents typically greater than 1 so that intermediate densities are unfavourable in compliance-based problems (typically $p_1, p_2 \geq 3$ in 2D problems, see Bendsøe and Sigmund 2004). The lower bound of the design variables, ρ_{min}, is a small positive value to prevent singularity issues. $\rho_{min} = 10^{-3}$ is assumed here.

In the case that the objective is to obtain designs presenting two distinct solid phases plus void (typical MMTO), the design variables ρ_1 and ρ_2 should touch their bounds at the end of the design iterations. In this case, depending on the combination of extreme values of ρ_1 and ρ_2, a unique phase is selected, see Fig. 1. In this setting, the design variable ρ_1 works as a topological variable as it identifies presence or absence of solid phase, and the design variable ρ_2 is responsible for material selection.

In case that the objective is to obtain FGM microstructures, p_1 and p_2 in (7) must be carefully chosen to accommodate desired penalization effects and consistency with the physics of solid mixtures. In this setting, intermediate values of the design variable ρ_1 are unfavorable such that void and solid regions can be identified. Additionally, intermediate values of ρ_2, which sets the proportion of each solid phase ($\mathbf{E}_1$ and $\mathbf{E}_2$) in the resulting solid mixture, must be consistent with the bounds provided for the effective elastic moduli of multiphase materials, e.g., the Hashin-Shtrikman (HS) bounds (Hashin and Shtrikman 1963). These are upper and lower bounds for the elastic moduli of composite materials depending on the volume fractions of each constituent materials, and it is assumed that these materials are mixed uniformly with no microstructure. Assuming the 2D case and that both materials are isotropic, as well as their mixture, with the

same Poisson's ratio, equal to 1/3, the HS bounds can be expressed as (see also Bendsøe and Sigmund 1999; Xia and Wang 2008)

$$E_{HS}^{-} = \frac{(2+\rho)E_1 + (1-\rho)E_2}{2(1-\rho)E_1 + (1+2\rho)E_2} E_2 \tag{8}$$

$$E_{HS}^{+} = \frac{\rho E_1 + (3-\rho)E_2}{(3-2\rho)E_1 + 2\rho E_2} E_1 \tag{9}$$

where E_{HS}^{-} and E_{HS}^{+} are respectively the lower and upper HS bounds. The volume fraction of the stiffest constituent material E_1 (Young's Modulus) is given by $\rho \in [0,1]$, while the volume fraction of the softest constituent material E_2 is given by $1-\rho$. The HS bounds are plotted in Fig. 2 to check how the interpolation law (7), function of ρ_2 only (one sets $\rho_1 = 1$), compares with HS bounds. In Fig. 2, different values of exponent p_2 are tested to investigate curve fitting.

From Fig. 2 is seen that, mixing two different isotropic solids, the resulting elastic properties do not linearly correlate with the volume fraction of each constituent. Therefore, to adequately capture FGM properties, the interpolation scheme predictions must be within the HS bounds for the entire volume fraction range. It is clearly observed that p_2 value must be comprised between 1 and 2. A value of 1.6 seems to render a good enough approximation in the scope of a Power-law based interpolation scheme. In fact, the match is not perfect as seen for some volume fractions. For low and high ρ values the bounds are slightly violated. The proposed value, $p_2 = 1.6$, is kind of a trade-off that avoids violating too much the bounds either for lower or higher ρ values. For an improved fitting, one might use another scheme, e.g., the average of the two HS bounds (Xia and Wang 2008). In terms of physics that strategy is sound, but it introduces much more mathematical complexity especially when it comes to sensitivity analysis. As a Power-law mimics just that, without much loss of accuracy, and it is mathematically much simpler, one proceeds with (7) in this work.

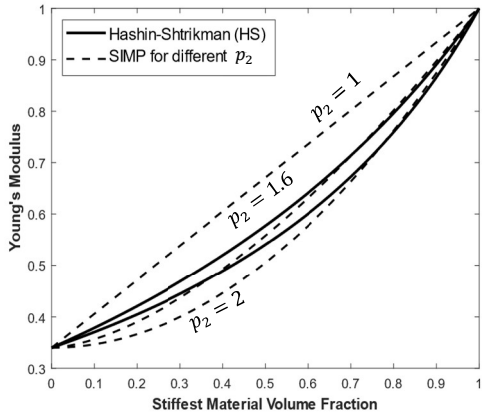

Fig. 2 Plot comparing the HS bounds with the SIMP interpolation scheme interpolating two isotropic solids using different values of exponent p_2

To sum up, the material model used here is a twofold one. As explained, it models either a composite material comprised by two discrete solids (conventional composite) or a mixture of two solids (advanced composite, FGM), plus void. Furthermore, the model assumes: linear elasticity; perfectly bonded solid phases; ductile solids such that failure can be predicted by the von Mises stress criterion.

3. Topology optimization framework

Conventional TO solves a single-material distribution problem over the domain Ω, favouring "black-white" designs. In fact, the TO problem is discrete or binary by nature. A widely known approach to relax this problem to the continuum, making it differentiable, is introducing density-based design variables. This way gradient-based optimization algorithms can search for the optimum. Among them, the MMA (Svanberg 1987) has become very popular as it uses approximations with the attractive features of convexity and separability. It manages well high number of design variables combined with a low to moderate number of design constraints. Since this work increases not only the number of variables, needed for material selection, but also the number of constraints, to control stresses locally, the MMA effectiveness can be questioned. In fact, recent attention has been given to handle stresses as they are, local, i.e., pursuing stress aggregation-free approaches, see e.g., Giraldo-Londoño et al. (2021a, 2021b), Senhora et al. (2020) and da Silva et al. (2020, 2021). As detailed thereafter, to handle TO problem formulations minimizing peak stresses in microstructural design, having as many stress constraints as the number of FE in the mesh, the authors here still propose using the common TO framework with design updates by MMA. To that purpose, a parallelized version of MMA is proposed to speedup treatment of an increased number of constraints comparing to what has been reported in the literature.

To avoid numerical problems, such as checkerboard patterns and mesh dependence, a density-based filtering technique is used here (Bruns and Tortorelli 2001), i.e.,

$$\tilde{\rho}_i = \frac{\sum_{j \in N_i} \max\{0, R_{min} - \|y_j - y_i\|\}\, \rho_j}{\sum_{j \in N_i} \max\{0, R_{min} - \|y_j - y_i\|\}} \tag{10}$$

where $\tilde{\rho}$ is the filtered density, N_i defines the respective set of elements neighbouring element i, the norm $\|y_j - y_i\|$ sets the spatial distance between elements i and j centroids, and R_{min} is the filter radius. This technique is applied to both design variables, $\boldsymbol{\rho}_1$ and $\boldsymbol{\rho}_2$, each one assumed uniform within each FE. Thereafter, the corresponding filtered densities $\tilde{\boldsymbol{\rho}}_1$ and $\tilde{\boldsymbol{\rho}}_2$ are the ones that define the UC layout, i.e., the previous formulae in Section 2 are to be interpreted as depending on filtered densities. The original design variables $\boldsymbol{\rho}$ have no physical meaning. Regarding the stress fields, the density filter also promotes a smoothness on the stress distributions at boundaries between two phases, preventing the so-called singularities (unphysical stresses), see Coelho et al. (2019).

In this work, one shows that multi-material designs can be stiffer and/or stronger than the single-material counterparts. To that purpose, TO problems are formulated in Section 3.1. The respective stress derivatives must be evaluated. The increased amount of calculus in the multi-material setting, that demands dealing with extra variables and constraints justifies here resorting to parallel techniques to reduce the cost of the time-consuming task of sensitivity analysis, as discussed in Section 3.2. Finally, Section 3.3 details a parallelization technique to handle a high number (thousands) of design constraints in MMA, local stress constraints in this case.

3.1. Problems formulation

Two different TO problems are formulated. The compliance-based problem (Section 3.1.1) that is solved in the context of MMTO and compared to SMTO. The stress-based problem (Section 3.1.2) that is solved in the context of both MMTO and FGMTO, and compared to SMTO as well.

3.1.1. Compliance-based MMTO

Compliance C is minimized subject to (s.t.) mass and/or material volume constraints. In the context of SMTO the mass and volume fraction constraints are equivalent. However, in MMTO, different materials have different mass density ρ^*. Therefore, the compliance-based MMTO problem, with two solids plus void, is formulated as follows:

$$\min_{\boldsymbol{\rho_1},\boldsymbol{\rho_2}} \quad C(\tilde{\boldsymbol{\rho}}_1, \tilde{\boldsymbol{\rho}}_2) = \frac{1}{2}\langle\boldsymbol{\sigma}\rangle\mathbf{C}^{\mathbf{H}}\langle\boldsymbol{\sigma}\rangle|\mathrm{Y}| \tag{11a}$$

$$\text{s.t.} \quad \frac{m}{m^*} = \frac{\sum_{e=1}^{n^e}[\tilde{\rho}_{1,e}(\tilde{\rho}_{2,e}\rho_1^* + (1-\tilde{\rho}_{2,e})\rho_2^*)|\mathrm{Y_e}|]}{m^*} \leq 1 \tag{11b}$$

$$\frac{V}{V^*} = \frac{\sum_{e=1}^{n^e}[\tilde{\rho}_{1,e}|\mathrm{Y_e}|]}{V^*} \leq 1 \tag{11c}$$

where the design variables ρ_1 and ρ_2 are within the intervals defined in Section 2.2; m is the effective mass, which interpolates, at each FE, mass densities ρ^* and void in a similar manner to (7) with $p_1 = p_2 = 1$; m^* is an upper bound on m; V is the material volume fraction with an upper bound V^*; and n^e is the total number of elements present in the FE mesh. When solving the MMTO problem (11), one seeks the stiffest design for a given mass and/or volume requirement.

3.1.2. Stress-based MMTO and FGMTO

In this work, the minimization of the maximum von Mises stress σ_e^{VM} is sought. However, a min-max problem raises non-differentiability issues. To overcome these issues, the so-called "bound formulation" is used here (Taylor and Bendsøe 1984; Coelho et al. 2021). This means replacing the original min-max stress problem by the problem of minimizing a variable z subject to stress constraints bounded by z, i.e., $\sigma_e^{VM} < z$. The bound z is an additional design variable that replaces the non-differentiable functional, $\max \sigma_e^{VM}$, and $z \in]0,+\infty[$.

The proposed stress-based MMTO, with two solids plus void, is formulated as:

$$\min_{\boldsymbol{\rho_1},\boldsymbol{\rho_2},z} \quad z \tag{12a}$$

$$\text{s.t.} \quad \frac{\sigma_e^{VM}}{z} \leq 1 \quad , \quad e = 1, \dots, n^e \tag{12b}$$

$$\frac{C}{C^*} \leq 1 \tag{12c}$$

$$\frac{V}{V^*} \leq 1 \tag{12d}$$

$$\frac{m}{m^*} \leq 1 \tag{12e}$$

$$\frac{\varphi_1 - \zeta_1}{\zeta_1} = \frac{\sum_{e=1}^{n^e}[(1-\tilde{\rho}_{1,e})(\tilde{\rho}_{1,e} - \rho_{min})] - \zeta_1}{\zeta_1} \leq 1 \tag{12f}$$

$$\frac{\varphi_2 - \zeta_2}{\zeta_2} = \frac{\sum_{e=1}^{n^e}[(1-\tilde{\rho}_{2,e})(\tilde{\rho}_{2,e} - \rho_{min})] - \zeta_2}{\zeta_2} \leq 1 \tag{12g}$$

where the design variables ρ_1 and ρ_2 are within the intervals defined in Section 2.2; C^* is a compliance upper bound; V^* and m^* are limits on volume fraction V and effective mass m, respectively, as defined in (11); φ_1 and φ_2 measure the level of intermediate values (gray) present on filtered density fields $\tilde{\boldsymbol{\rho}}_1$ and $\tilde{\boldsymbol{\rho}}_2$, and $\zeta_1 \in]0,+\infty]$ and $\zeta_2 \in]0,+\infty]$ are their respective upper bounds, to be kept small. The constraints in formulations (11) and (12) are written in the format to be read by MMA (Fortran version).

The bound C^* in (12c) is used to ensure that the resulting design is stiff enough, i.e., connectivity of the solid phase exists, and the trivial solutions of uniform intermediate density or structure absence are avoided (Sigmund and Maute 2013; Bruggi and Duysinx 2012). In the context of MMTO, one expects that the optimal design obtained through (12) presents discrete material phases. To that purpose, the presence of intermediate densities (gray) is penalized through the exponents in (7). However, this may not suffice in strength-oriented design. That is why constraints (12f) and (12g) are added here. Bear in mind that, the averaging imposed by filter (10), necessarily opens an exception regarding the presence of gray. Gray always appears at the border of each two neighboring phases. In fact, such border looks like a bit blurred as shown later in Section 4. Hence, careful choice of parameters ζ_1 and ζ_2 is demanded which, comprehensively, can be problem dependent. To illustrate, for high material volume fractions, ζ_1 and ζ_2 are possibly lower comparing to low material volume fractions. The reason why is that higher material volume fractions may exhibit interfaces between phases with less perimeter and thus less gray appears. Results in Section 4 show this trend. Adjusting such parameters may thus require running the optimization problem more than once to get insight. In general, it is good to start not having such ζ bounds too tight. Then they must become gradually smaller by means of a continuation approach such that at the end of the design iterations their values are small enough to evidence shaper interfaces which facilitates design interpretation.

Regarding the stress constraints present in (12b), the bound z is both the design variable and the objective to be minimized. Here, there is no interpolation among different material yielding stresses depending on the materials present in the pool for selection. Such formulation is beyond the scope of the present work, but it might be interesting to explore it in the future as it also benefits engineering practice. In the present framework, one seeks instead the optimal spatial distribution of two solids amidst void to reduce the peak stress. Considering previous experience from the authors in Coelho et al. (2021), no particular stress relaxation is applied, *qp*-approach (Bruggi 2008) or *epson*-relaxation (Duysinx and Bendsøe 1998). Even so, the algorithm is able to remove material while solving (12). To sum up, the stress-based MMTO aims here to find multi-material designs, with multiple discrete solid phases, which are optimal in terms of strength, for compliance, volume fraction and/or mass requirements.

The stress-based FGMTO problem formulation is very similar to the MMTO case. FGM designs are achieved here by interpolating the two solids according to Fig. 2, as explained in Section 2.2. The intermediate density values of $\widetilde{\boldsymbol{\rho}}_2$ have physical meaning now, as they represent different proportions of each solid present in the mixture. Therefore, the constraint (12g) is not used. However, the intermediate values of $\widetilde{\boldsymbol{\rho}}_1$ remain penalized, such that solid-void regions can be obtained, i.e., constraint (12f) must be kept.

3.2. Sensitivity analysis

Since problems (11) and (12) are to be solved through a gradient-based algorithm (MMA), first order derivates of all functions need to be computed. The sensitivity of a given function, say g, w.r.t. a design variable $\boldsymbol{\rho}$, depends on the respective filtered density $\widetilde{\boldsymbol{\rho}}$ by applying the chain rule (see Sigmund 2007):

$$\frac{\mathrm{d}g}{\mathrm{d}\rho_e} = \sum_{i \in N_e} \frac{\partial g}{\partial \tilde{\rho}_i} \frac{\mathrm{d}\tilde{\rho}_i}{\mathrm{d}\rho_e} = \sum_{i \in N_e} \frac{\partial g}{\partial \tilde{\rho}_i} \left[\frac{R_{min} - \|y_e - y_i\|}{\sum_{j \in N_i} \max\{0, R_{min} - \|y_j - y_i\|\}} \right] \tag{13}$$

where index e refers to the finite element e.

The required gradients in (13) w.r.t. $\tilde{\rho}_{j,i}$ to solve problems (11) and (12) are shown as follows. Keep in mind below that index $j \in \{1,2\}$ defines the corresponding density field (i.e., $\widetilde{\boldsymbol{\rho}}_{\mathbf{1}}$ or $\widetilde{\boldsymbol{\rho}}_{\mathbf{2}}$), indexes $i, e \in \{1, \dots, n^e\}$ correspond to the FE index, and index $l \in \{1,2\}$ defines the respective functions ζ_1 and ζ_2. The compliance derivative is,

$$\frac{\mathrm{d}C}{\mathrm{d}\widetilde{\boldsymbol{\rho}}} = -\frac{1}{2}\langle\boldsymbol{\sigma}\rangle\mathbf{C}^{\mathrm{H}}\frac{\partial\mathbf{E}^{\mathrm{H}}}{\partial\widetilde{\boldsymbol{\rho}}}\mathbf{C}^{\mathrm{H}}\langle\boldsymbol{\sigma}\rangle|\mathrm{Y}| \tag{14}$$

The volume derivative is,

$$\frac{\mathrm{d}V}{\mathrm{d}\tilde{\rho}_{j,i}} = \begin{cases} |\mathrm{Y}_i| & \text{if } j = 1 \\ 0 & \text{if } j = 2 \end{cases} \tag{15}$$

The mass derivative is,

$$\frac{\mathrm{d}m}{\mathrm{d}\tilde{\rho}_{j,i}} = \begin{cases} \left(\tilde{\rho}_{2,i}\rho_1^* + \left(1-\tilde{\rho}_{2,i}\right)\rho_2^*\right)|\mathrm{Y}_i| & \text{if } j = 1 \\ \tilde{\rho}_{1,i}(\rho_1^* - \rho_2^*)|\mathrm{Y}_i| & \text{if } j = 2 \end{cases} \tag{16}$$

The penalization function φ derivative is,

$$\frac{\mathrm{d}\varphi_l}{\mathrm{d}\tilde{\rho}_{j,i}} = \begin{cases} -2\tilde{\rho}_{j,i} + \rho_{min} + 1 & \text{if } j = l \\ 0 & \text{if } j \neq l \end{cases} \tag{17}$$

The von Mises stress derivative is,

$$\frac{\mathrm{d}\sigma_e^{VM}}{\mathrm{d}\tilde{\rho}_{j,i}} = \frac{\partial\sigma_e^{VM}}{\partial\tilde{\rho}_{j,i}} + \frac{\partial\sigma_e^{VM}}{\partial\chi_k^{mn}}\frac{\mathrm{d}\chi_k^{mn}}{\mathrm{d}\tilde{\rho}_{j,i}} \tag{18}$$

In (14), the derivative of the homogenized stiffness tensor w.r.t. density field $\tilde{\rho}_{j,i}$, can be easily evaluated solving a self-adjoint problem as explained in Bendsøe and Sigmund (2004), which gives the following result:

$$\frac{\partial E_{nlkm}^{\mathrm{H}}}{\partial\tilde{\rho}_{j,i}} = \frac{1}{|\mathrm{Y}|}\int_{\mathrm{Y}_i}\frac{\partial E_{pqrs}}{\partial\tilde{\rho}_{j,i}}\left(\delta_{pk}\delta_{qm} - \frac{\partial\chi_p^{km}}{\partial y_q}\right)\left(\delta_{rn}\delta_{sl} - \frac{\partial\chi_r^{nl}}{\partial y_s}\right)\mathrm{dY} \tag{19}$$

The total derivatives of the von Mises stresses in (18) depend explicitly and implicitly (through the solution $\boldsymbol{\chi}$ of the homogenization equations) on the design variable $\tilde{\rho}_{j,i}$. To compute these derivatives, the adjoint method is used, see Haug et al. (1986). The computation of these derivatives was previously addressed in Collet et al. (2018) and Coelho et al. (2021) for an applied average strain and stress, respectively, and considering SMTO. Here, they are extended to the MMTO case.

In general, sensitivity is a time-consuming task. Here, the total number of stress constraints equals the total number of finite elements considered. This means stresses are treated as they are, local, but that also means many problem constraints. Furthermore, each function requires derivatives w.r.t. all density variables. Comparing to SMTO, the number of these variables doubles in the MMTO and FGMTO cases considered here, as two density fields exist. The authors pursue a Fortran programming implementation of this sensitivity analysis. The computations involve nested loops. Basically, two main loops. An outer loop through all constraints and an inner loop through all density variables. Notice that the sensitivity evaluation of each stress constraint is independent of another. To speed up the computational time spent here, the code is parallelized resorting to OpenMP directives for Fortran. The parallel implementation considered here splits the outer loop into several parts, each one handled by a different processor (see Appendix).

The total derivatives of χ_k^{rs} w.r.t. $\tilde{\rho}_{j,i}$ in (18) are obtained differentiating the equilibrium equations of the local homogenization problem (2) in its FE or discrete form $\mathbf{K}\boldsymbol{\chi} = \mathbf{F}$. Therefore, (18) can be rewritten as:

$$\frac{\mathrm{d}\sigma_e^{VM}}{\mathrm{d}\tilde{\boldsymbol{\rho}}} = \frac{\partial \sigma_e^{VM}}{\partial \tilde{\boldsymbol{\rho}}} + \boldsymbol{\lambda}^{\mathsf{T}} \left[\frac{\partial \mathbf{F}}{\partial \tilde{\boldsymbol{\rho}}} - \frac{\partial \mathbf{K}}{\partial \tilde{\boldsymbol{\rho}}} \boldsymbol{\chi} \right] \tag{20}$$

where $\boldsymbol{\lambda}$ is solution of the following adjoint problem:

$$\mathbf{K}\boldsymbol{\lambda} = \left(\frac{\partial \sigma_e^{VM}}{\partial \boldsymbol{\chi}} \right)^{\mathsf{T}} \tag{21}$$

The required partial derivatives of the stress σ_e^{VM} defined in (6), w.r.t. both $\tilde{\rho}_{j,i}$ and χ_k^{rs}, need the following derivatives of the micro stresses σ_{zy}^e defined in (3-4), given an average stress tensor $\langle \sigma_{pq} \rangle$,

$$\begin{aligned} \frac{\partial \sigma_{zy}^e}{\partial \tilde{\rho}_{j,i}} &= \frac{\partial E_{zykm}}{\partial \tilde{\rho}_{j,i}} \left(\delta_{kr}\delta_{ms} - \frac{\partial \chi_k^{rs}}{\partial y_m} \right) C_{rspq}^{\mathrm{H}} \langle \sigma_{pq} \rangle \delta_{ie} \\ &- E_{zykm} \left(\delta_{kr}\delta_{ms} - \frac{\partial \chi_k^{rs}}{\partial y_m} \right) C_{rstu}^{\mathrm{H}} \frac{\partial E_{tuhv}^{\mathrm{H}}}{\partial \tilde{\rho}_{j,i}} C_{hvpq}^{\mathrm{H}} \langle \sigma_{pq} \rangle \end{aligned} \tag{22}$$

$$\frac{\partial \sigma_{zy}^e}{\partial \chi_{kn}^{rs}} = -E_{zykm} \frac{\partial \psi_n^e}{\partial y_m} C_{rspq}^{\mathrm{H}} \langle \sigma_{pq} \rangle \tag{23}$$

where ψ_n^e are the FE shape functions, and the derivatives of the homogenized stiffness tensor $\mathbf{E}^{\mathrm{H}}$ simply involve the derivative of (7) to be inserted in (19). Lastly, the derivatives w.r.t. the design variable z are trivial and therefore skipped here.

3.3. MMA parallelization

Mainly the large number of stress constraints in (12), makes the optimizer (MMA) an important bottleneck in the present work, when it fully runs in serial. That may discourage its use. Therefore, the authors propose a MMA parallel framework with important speedups when many constraints are treated. In Aage and Lazarov (2013), the Message Passing Interface (MPI, Gropp et al. 1999) is used to propose a MMA parallel framework dealing well with huge number of design variables. Recall here that one considers in (12) two design variables per FE, but more variables could be considered in case more phases are interpolated. MPI is undoubtedly suitable for distributed-memory computer architectures. In the case of shared-memory architectures, OpenMP is the most suitable protocol for code parallelization since, unlike MPI, no communications through "send" and "receive" calls among processors are required (Dagum and Menon 1998). This is the main reason driving here the authors to propose an alternative parallel version of MMA to be used in shared-memory architectures and when thousands of constraints are treated (see Appendix).

Briefly, what MMA does, according to the original version (Svanberg 1987), is solving a sequence of approximate sub-problems, rather than solving the original non-linear optimization problem. The original objective and constraint functions are replaced by approximate convex and separable functions. The MMA sub-problem is convex and separable, meaning that a dual method can be used for its solution. The first step of this method consists in constructing the Augmented

Lagrangian $\mathcal{L}$ of the sub-problem, defining then the dual objective function Ψ, as seen in Svanberg (1987). The unique solution x_j of the dual objective function Ψ is obtained solving $\partial\mathcal{L}/\partial x_j = 0$, which gives the following explicit expression for $x_j(\lambda_i)$:

$$x_j(\lambda_i) = \frac{\left(p_{0j} + \sum_{i=1}^{m}(\lambda_i p_{ij})\right)^{\frac{1}{2}} L_j + \left(q_{0j} + \sum_{i=1}^{m}(\lambda_i q_{ij})\right)^{\frac{1}{2}} U_j}{\left(p_{0j} + \sum_{i=1}^{m}(\lambda_i p_{ij})\right)^{\frac{1}{2}} + \left(q_{0j} + \sum_{i=1}^{m}(\lambda_i q_{ij})\right)^{\frac{1}{2}}} \tag{24}$$

where λ_i are the so-called "dual variables", L_j and U_j are the lower and upper asymptotes, respectively. Therefore, one can write the explicit expression for the dual objective function as $\Psi(\lambda_i) = \mathcal{L}\big(x_j(\lambda_i), \lambda_i\big)$. The derivatives of $\Psi(\lambda_i)$, w.r.t. the dual variables λ_i, are given by:

$$\frac{\partial\Psi(\lambda_i)}{\partial\lambda_i} = \sum_{j=1}^{n}\left(\frac{p_{ij}}{U_j - x_j(\lambda_i)} + \frac{q_{ij}}{x_j(\lambda_i) - L_j}\right) - y_i - b_i \tag{25}$$

where details about coefficients p_{ij}, q_{ij}, y_i and b_i can be found in Svanberg (1987).

The dual problem is solved by the steepest ascent method, in the first two iterations, followed by the Newton's method. Regardless of the method, once the search direction is found, a line search is carried out to find the next point. This iterative process ends when a specified convergence tolerance is met. Once the dual problem has been solved, the optimal solution of the "primal" sub-problem is obtained through (24), for the obtained optimal dual solution $\boldsymbol{\lambda}^*$.

Finding the solution of the dual problem requires computing (24) and (25) several times. Therefore, parallel computing can be conveniently applied to these parts of MMA code. Equations (24) and (25) are programmed in MMA Fortran subroutines `XYZLAM` and `GRADI`, respectively. Each one involves nested loops, being the outer loop parallelized here. In (24) it corresponds to $j = 1, \dots, n$ (number of primal variables) and in (25) corresponds to $i = 1, \dots, m$ (number of dual variables).

Another important part to be parallelized is the Newton's method itself, as it iterates a lot. The method implies setting and solving repeatedly the following system of equations, which can be expensive:

$$\mathbf{H}(\boldsymbol{\lambda})\mathbf{d} = \frac{\partial\Psi(\boldsymbol{\lambda})}{\partial\boldsymbol{\lambda}} \tag{26}$$

where $\mathbf{H}(\boldsymbol{\lambda})$ is the Hessian matrix of the dual objective function and $\mathbf{d}$ is the search direction sought. Using results from Lagrangian duality (see Luenberger and Ye 1984), the Hessian can be computed as:

$$\mathbf{H} = -\frac{\partial}{\partial x_j}\left(\frac{\partial\Psi(\lambda_i)}{\partial\lambda_i}\right)\left[\frac{\partial^2\mathcal{L}}{\partial {x_j}^2}\right]^{-1}\left(\frac{\partial}{\partial x_j}\left(\frac{\partial\Psi(\lambda_i)}{\partial\lambda_i}\right)\right)^{\mathsf{T}} \tag{27}$$

where

$$\frac{\partial}{\partial x_j}\left(\frac{\partial\Psi(\lambda_i)}{\partial\lambda_i}\right) = \frac{p_{ij}}{\left(U_j - x_j\right)^2} - \frac{q_{ij}}{\left(x_j - L_j\right)^2} \tag{28}$$

and

$$\frac{\partial^2\mathcal{L}}{\partial {x_j}^2} = \frac{2\left(p_{0j} + \sum_{i=1}^{m}(\lambda_i p_{ij})\right)}{\left(U_j - x_j\right)^3} + \frac{2\left(q_{0j} + \sum_{i=1}^{m}(\lambda_i q_{ij})\right)}{\left(x_j - L_j\right)^3} \tag{29}$$

The Hessian matrix construction is carried out in MMA Fortran subroutine `HESSI`, and it can be expensive as it involves nested loops in each iteration of Newton's method. The outer loop corresponds to the index $j = 1, \dots, n$ and the inner loop corresponds to the index $i = 1, \dots, m$. The Hessian dimension is equal to the number β of "free" dual variables, i.e., dual variables λ_i that correspond to $y_i > 0$ in MMA subproblem. Comprehensively, this dimension can change during the iterative process of solving the dual problem. This is an active set constraints strategy which is helpful in case a relatively small number of constraints are active. However, in MMTO and FGMTO one expects a high number of active ones. Hence, for the construction of Hessian matrices with dimension $\beta \geq 100$, parallel computing is used here. It is important to notice that this parallelization is only possible due to the OpenMP directive `!$OMP ATOMIC` that prevents several processors from overwriting/updating the same memory location simultaneously (see Appendix).

Finally, to solve the system of equations (26) one takes advantage of LAPACK routines available in Intel® oneAPI Math Kernel Library (oneMKL). These are efficient routines that support parallel computing. Here one uses the driver routine `DPPSV` that solves the system of linear equations, $\mathbf{Ax} = \mathbf{B}$, where $\mathbf{A}$ is a symmetric positive definite packed matrix using Cholesky decomposition. The parallel version of this routine here is only used for system of equations with dimensions $\beta \geq 1000$.

4. Results

The solid material phases (stiff and weak) selected for the examples that follow are presented in Table 1. To simplify, the values of ratios E/E_{Steel} and $\rho^*/\rho^*_{\text{Steel}}$ (in bold) are here used as problem data for E [GPa] and ρ^* [kg/m^3], respectively, instead of the absolute values indicated. Interestingly, this normalization also highlights that Young's Modulus ratios and mass densities ratios between engineering alloys are similar, see Ashby (1999). A Poisson ratio of 0.3 is assumed for both solids. Results are obtained for three different prescribed macroscopic (average) stress tensors. The bulk-type load in (30) and two mixed loading cases, in (31) and (32).

$$\langle \boldsymbol{\sigma}_1 \rangle = \begin{bmatrix} -1 & 0 \\ 0 & -1 \end{bmatrix} \quad [\text{MPa}] \tag{30}$$

$$\langle \boldsymbol{\sigma}_2 \rangle = \begin{bmatrix} -1 & -0.1 \\ -0.1 & -0.5 \end{bmatrix} [\text{MPa}] \tag{31}$$

$$\langle \boldsymbol{\sigma}_3 \rangle = \begin{bmatrix} -1 & 0.1 \\ 0.1 & 0.5 \end{bmatrix} \quad [\text{MPa}] \tag{32}$$

Table 1 Material properties of Steel (stiff solid) and Aluminium (weak solid). Property ratios highlighted in bold

Materials	E [GPa]	E/E_{Steel}	ρ^* [kg/m^3]	$\rho^*/\rho^*_{\text{Steel}}$
Steel	200	**1**	7900	**1**
Aluminium	68	**0.34**	2700	**0.34**

Due to symmetry, only a quarter of the UC needs to be considered in the bulk case which is an advantage in terms of reducing the number of design variables and stress constraints. In contrast, the mixed loading cases require the full UC meshing and thus the computational cost increases considerably because of the same number of stress constraints and finite elements.

Typically, in SMTO, an active-set strategy reduces this cost (Coelho et al. 2021; Collet et al. 2018). However, in MMTO, stresses tend to be more evenly distributed, especially in the FGMTO case, which means that much more constraints become active. For example, the FGMTO results, as shown later, for the bulk case (with $V^* = 0.9$) and the last mixed loading case (with $V^* = 0.8$) have 2315 (out of 2500) and 3552 (out of 4096) active stress constraints, respectively. Hence, the active-set strategy savings can be questioned. Notice also that one needs an enlarged design space (two design variables per finite element) to interpolate between two solid phases plus void. Therefore, one conveniently resorts to parallel computing to reduce the computational cost (see Section 3 and Appendix).

The mesh discretization must balance well between accuracy and runtime. In Coelho et al. (2019), a 2D mesh convergence analysis in SMTO problems concludes that square-grid meshes between 64x64 and 128x128 are reasonable choices. Therefore, the results here are obtained on the top of 100×100 meshes for the bulk load case and 64×64 meshes for the mixed loading cases. The initial designs either exhibit a centered square or circle of low density surrounded by a higher density region.

This section is outlined as follows. Firstly, one addresses the bulk-type load in Section 4.1 performing a compliance-based MMTO (Section 4.1.1), a stress-based MMTO (Section 4.1.2) and a stress-based FGMTO (section 4.1.3). SMTO results are revisited for comparison purposes. Finally, the two mixed loading cases are addressed in Section 4.2 performing a compliance and stress-based SMTO (Section 4.2.1), a stress-based MMTO (Section 4.2.2) and a stress-based FGMTO (section 4.2.3).

4.1. Bulk-type load

Due to symmetry, results can be presented in quarters of the UC domain as shown in Fig. 3. The final topology is characterized by the **E** distribution, remember the colour map in Fig. 1. In multi-material designs the individual density fields are plotted next to each other for comprehension. Notice that the density field $\boldsymbol{\rho}_2$ is only meaningful in FEs where $\boldsymbol{\rho}_1 = 1$, see (7).

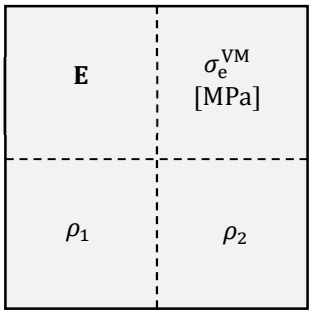

Fig. 3 Template chosen to present the multi-material results for the bulk-type load

4.1.1. Compliance-based MMTO

In this section, results of problem (11) are shown considering different upper bounds on mass and volume fraction, m^* and V^*, respectively. A continuation approach is applied to p_1 and p_2 in (7), i.e., $p_1 = p_2 = 2 \rightarrow 4$ during the first 20 design iterations for all m^* considered, exception made to the $m^* = 0.9$ where such gradual increment takes 40 iterations.

The compliance-based MMTO problem with only a volume constraint always privileges selection of the stiffest materials available, which is trivial and thus skipped here. Here, one imposes a global mass constraint with $m^* \in \{0.6; 0.7; 0.8; 0.9\}$. Fig. 4 (top) shows the SMTO results for these mass thresholds when only steel is used. In this case (11b) and (11c) coincide, as $\tilde{\rho}_2 = \rho^* = 1$. The optimal layout change from a square-type into a circle, across different volume fractions, is consistent with the Vigdergauz results (Vigdergauz 2001, 2002). These results can be compared to the MMTO results shown in Fig. 4 (bottom), obtained for the same mass, i.e., only constraint (11b) exists as the total volume fraction is free. The multi-material case mixes the stiff and weak solids to the point of eliminating the original void. This results in a non-porous composite where the stiffer phase embraces the weaker phase. Table 2 presents all the compliance values, the steel volume fraction V_{Steel} in MMTO designs, and the percentage δ that shows how less compliant the multi-material design is comparing to SMTO. So, material combinations can outperform here hole openings. In fact, for compliance and mass (or weight) performances, regardless which one is constrained, the other one, as an objective, can be further reduced in the multi-material setting.

Comparing the top and bottom stress plots in Fig. 4, see the stress scale in between, one can conclude that MMTO not only lowers compliance but also the von Mises stress (at least in 40%). However, as previously studied in Coelho et al. (2019, 2021), the stress-based formulation is best adequate to find equi-stress holes (ESP) comparing to the compliance-based, as compliance is a quite flat function and rather insensitive to local stress changes. This explains some lack of equi-stressness (unevenly distribution of stresses) seen in the stress plot of Fig. 4 (top), compare to Fig. 6 (top), being the peak stress there higher than the theoretical value (minimum) obtained through $\sigma_{t|\Gamma} = \text{tr}\langle\boldsymbol{\sigma}\rangle/V$.

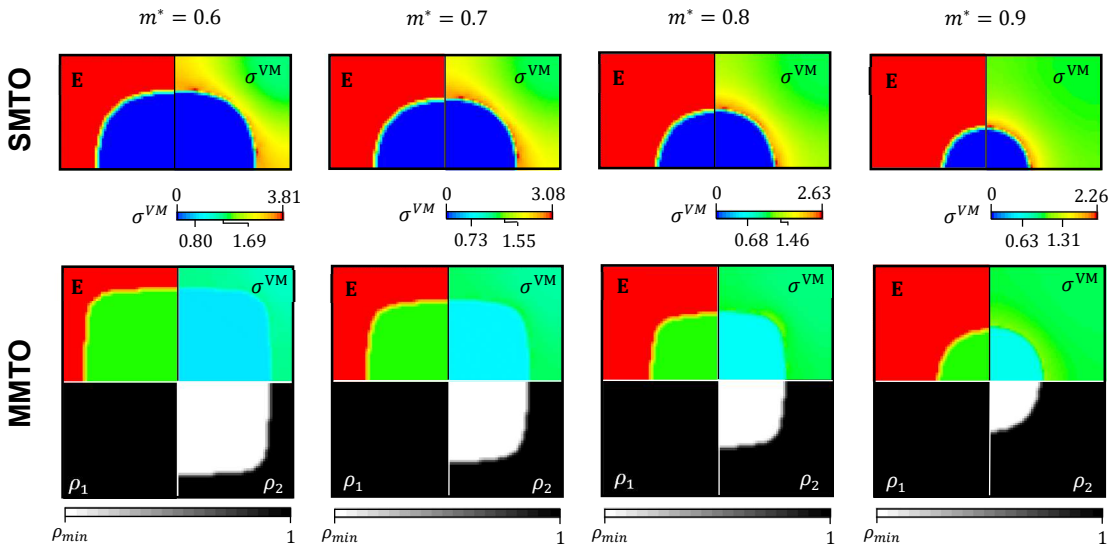

Fig. 4 SMTO (top) and MMTO (bottom) results for compliance minimization with different mass thresholds. The lowest and highest stress values in SMTO and MMTO designs are indicated in the colour scale between pictures

Table 2 Compliance values [J] for the SMTO and MMTO results shown in Fig. 4

		m^*			
		0.6	0.7	0.8	0.9
SMTO	C	2133	1619	1239	944
MMTO	V_{Steel}	0.39	0.55	0.70	0.85
	C	1379	1171	995	839
δ [%]		**- 35,3**	**- 27.7**	**- 19.7**	**- 11.1**

In practice, certain engineering applications may require a porous composite material. In that case it is of interest solving (11) with mixed constraints. However, mass and volume upper bounds must be carefully chosen such that room is still found in MMTO to improve the compliance of SMTO. This means that if the SMTO design has mass m^{opt} (e.g., 0.6), which coincides with volume V^{opt} (e.g., 0.6), the MMTO problem with $m^* = m^{opt}$ must have at least $V^* > V^{opt}$ (e.g., 0.9). For these example values ($m^* = 0.6$ and $V^* = 0.9$), the MMTO compliance is 1558, which is above the prior MMTO result of 1379 but still below the SMTO compliance result of 2133. Fig. 5 shows the corresponding layout. It is the stiffer solid that embraces the hole and also notice that the peak stress is still below the SMTO case.

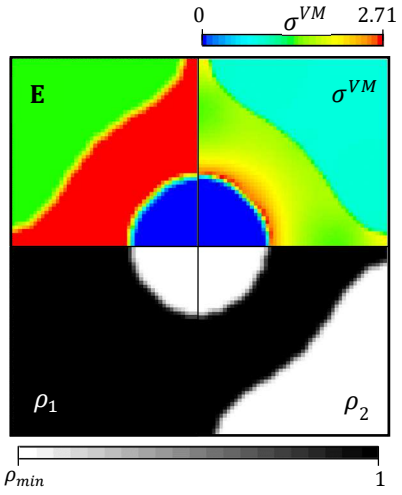

Fig. 5 Result for compliance-based MMTO with mass (m^* = 0.60) and volume (V^* = 0.90) constraints. Optimal compliance is 1558J and peak stress is 2.71MPa

4.1.2. Stress-based MMTO

Solving (12) with mass and compliance constraints, choosing as upper bounds the previous values in Section 4.1.1, one obtains the same plots of Fig. 4 (bottom) where stress improvements can already be recognized. Therefore, one now optimizes for different volume fraction limits, i.e., $V^* \in \{0.60; 0.70; 0.80; 0.90\}$. This way the original hole area in Fig. 4 (top) is not compromised. For each V^*, further stress reduction is possible in MMTO on account of introducing a more compliant second material phase. This means that the original compliance value, from SMTO, is now increased. To that purpose, the constraint (12c) is considered with a compliance limit C^* that

is 25% higher, compare compliance values in Table 3. Although compliance increases, its upper limit still ensures that the optimized solid part of the design domain is connected (the design is stiff enough). Even so, (12c) may not suffice to capture well-defined discrete phases, i.e., two solids plus void. Undoubtedly, the exponents p_1 and p_2 in (7) play an important penalization role. In MMTO here, these exponents are constant and equal to 4 during the optimization history. However, it can still be difficult to get rid of intermediate densities. In fact, "gray" is in favour of lowering stresses. In order to eliminate such "gray", one penalizes the intermediate values of $\boldsymbol{\rho}_1$ and $\boldsymbol{\rho}_2$ through (12f) and (12g), respectively. In these equations, ζ_1 and ζ_2 must be tuned and Table 4 presents their final values.

Interestingly, since $\rho_1^* = 1$, constraints (12e) and (12d) would coincide in case only solid $\mathbf{E}_1$ exists, i.e., V^* in (12d) would be also the total mass of Steel (St). In the MMTO case, the strategy pursued here is selecting a mass threshold m^* in (12e) such that $m^* < V^*$, which then enforces the presence of a certain amount of solid $\mathbf{E}_2$, Aluminum (Al). Considering the relationships $V^* = V_{St}^* + V_{Al}^*$, $m^* = \rho_{\mathrm{St}}^* V_{St}^* + \rho_{\mathrm{Al}}^* V_{Al}^*$ and the following data $\rho_{\mathrm{St}}^* = 1$, $\rho_{Al}^* = 0.34$, V_{Al}^*=0.1, after some algebra, one obtains $m^* = V^* - 0.066$ which justifies the m^* values presented in Table 3. Therefore, constraint (12e) can be interpreted as equivalent to the Aluminium volume fraction constraint with a minimum threshold of 10%, i.e., $V_{Al} \geq 0.1$. The rationale of using the mass constraint, instead of two volume fraction constraints, is to better highlight the fact that the obtained stress reduction comes also along with mass savings on account of more compliant designs, compared to SMTO, as highlighted in bold at the bottom of Table 3.

Table 3 Compliance [J], mass and stress [MPa] results for the SMTO and MMTO problems. Comparative study

		V^*			
		0.60	0.70	0.80	0.90
SMTO	C	2133	1619	1239	944
	m	$\equiv V^*$			
	$\sigma_{\max}^{\mathrm{VM}}$	3.40	2.83	2.40	2.04
MMTO	C	2632	2024	1520	1141
	m^*	0.534	0.634	0.734	0.834
	$\sigma_{\max}^{\mathrm{VM}}$	3.08	2.41	2.01	1.48
δ (%)	C	**+ 23.4**	**+ 25**	**+ 22.7**	**+ 20.9**
	m	**- 11**	**- 9.4**	**- 8.3**	**- 7.3**
	$\sigma_{\max}^{\mathrm{VM}}$	**- 9.41**	**- 14.8**	**- 16.3**	**- 27.4**

Table 4 Parameters ζ_1 and ζ_2 for each V^* considered in stress-based MMTO

	V^*			
	0.60	0.70	0.80	0.90
ζ_1	50	57	50	26
ζ_2	105	83	85	53

Ideally in multi-material optimization, numerical issues apart, the algorithm should be able to distribute softer solid $\mathbf{E}_2$ in the UC domain to reduce stresses without having its amount prescribed. This statement is supported by the authors' previous work where multi-material shape optimization is carried out, see Coelho et al. (2021). However, in the density-based MMTO case, allowing an extra solid phase, $\mathbf{E}_2$, implies increasing ζ_2 such that more "gray" can be accommodated. Bear in mind that including more phases in design means also more interface perimeter, i.e., it really means more "gray" presence because of density filtering. Therefore, the authors realize that unless a minimal amount of phase $\mathbf{E}_2$ be enforced, the algorithm simply finds a blurry transition between void and solid $\mathbf{E}_1$ resembling a FGM, as much as threshold ζ_2 allows. The FGM is really effective in stress mitigation as addressed in the next Section. However, in this Section, one aims discrete phases characterization, MMTO. Therefore, for the sake of a well-defined solid $\mathbf{E}_2$ presence, one proceeds adding the mass constraint as just justified above.

To avoid convergence issues some strategies are followed. A continuation approach that gradually decreases C^*, ζ_1 and ζ_2 values during the first design iterations is applied. The design variable z update is prevented from jumping too much by changing the ALBEFA parameter in MMA, i.e., ALBEFA $= 0.995 \rightarrow 0.5$ during the first design iterations.

Fig. 6 presents the results for MMTO and compares them to the SMTO results, these last ones are here recovered from Coelho et al. (2021). The stress-based SMTO results better capture the ESP, compare to Fig. 4 (top). The compliance and the maximum stress values between SMTO and MMTO can be compared in Table 3. The percentage δ summarizes how more compliant and lighter MMTO designs are, and how less stressed they are when compared to SMTO ones. Therefore, MMTO designs can be stronger and lighter than SMTO ones although more compliant for the same material volume fraction. Furthermore, higher material volume fractions have more potential in stress reduction. Finally, one representative case ($V^* = 0.7$) is selected as an example of the optimization history of the objective and constraint functions as well as the continuation approaches used for compliance and ζ values along design iterations, see Fig. 7.

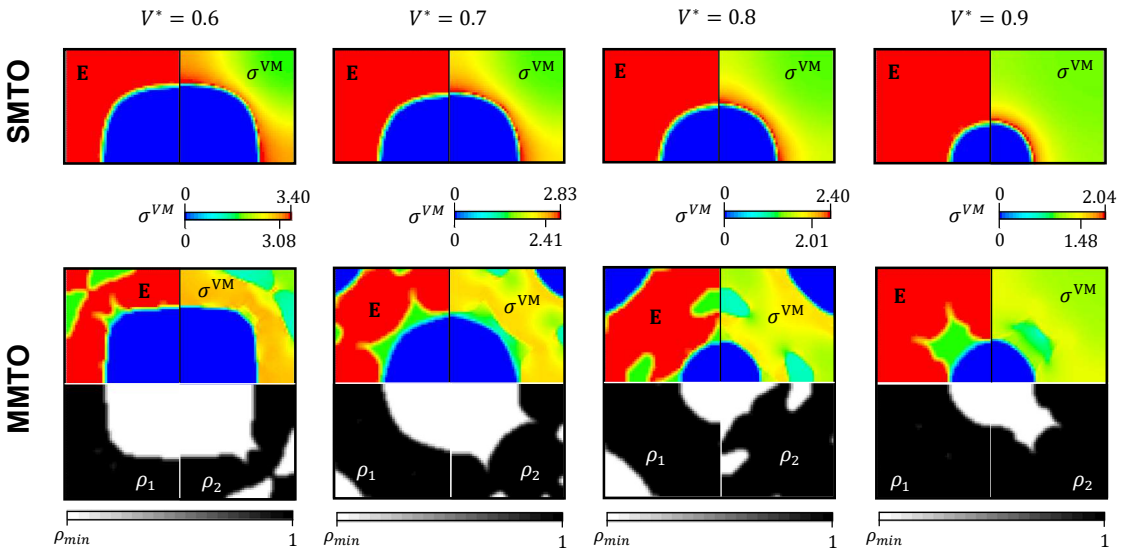

Fig. 6 Stress-based SMTO and MMTO results for different material volume fractions

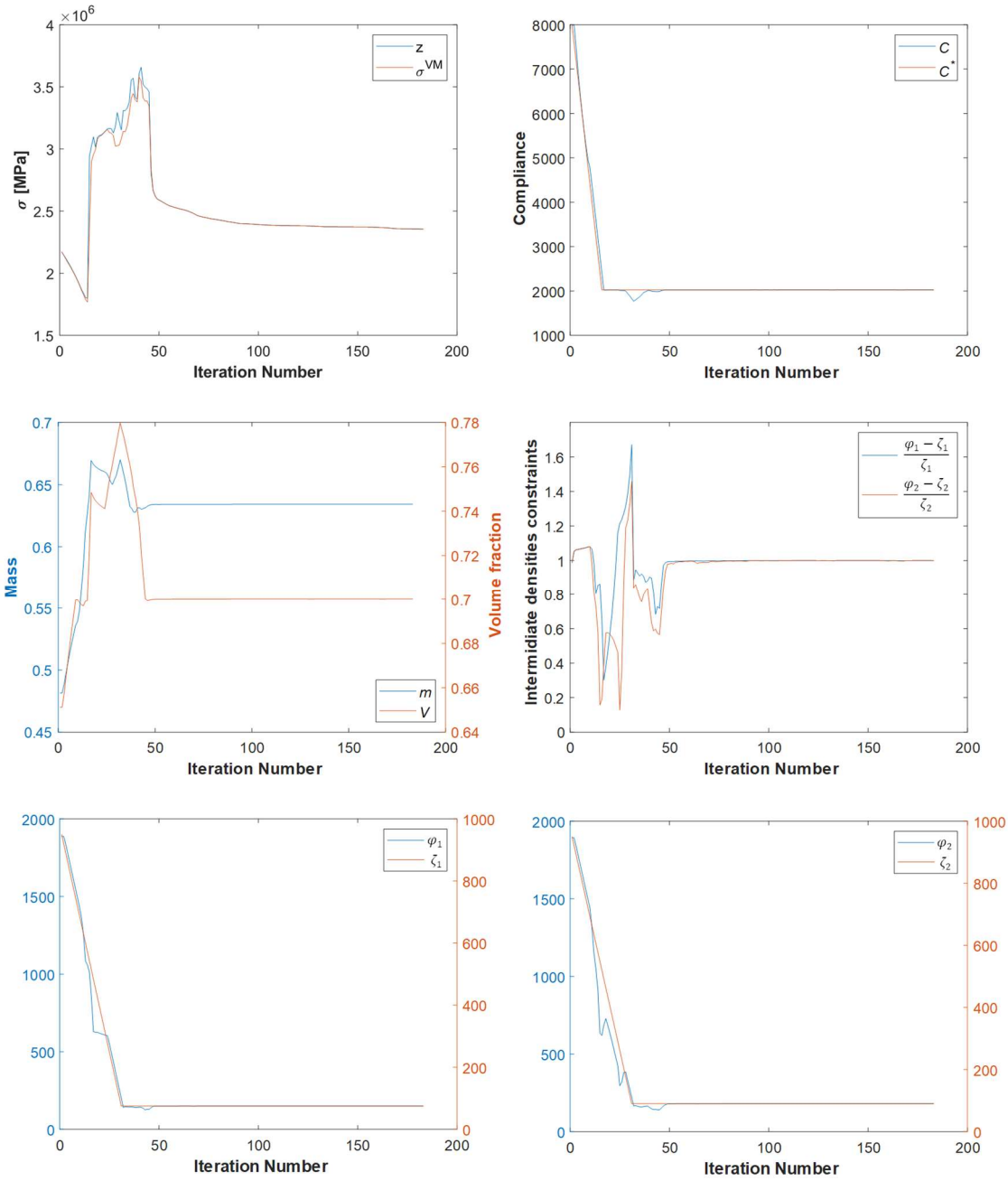

Fig. 7 Optimization history of the stress-based MMTO problem for $V^* = 0.70$

4.1.3. Stress-based FGMTO

Problem (12) here is simplified since constraints (12e) and (12g) are discarded. As in Section 4.1.2 one considers $V^* \in \{0.60; 0.70; 0.80; 0.90\}$ but now the compliance originally obtained in SMTO is worsened till 40%. Remind that the penalization exponents in (7) are now constant and equal to $p_1 = 4$ and $p_2 = 1.6$ (as explained in Section 2.2) throughout the optimization history. Intermediate values of $\boldsymbol{\rho}_1$ are penalized through (12f) with $\zeta_1 \in \{80; 70; 60; 50\}$ for the respective V^* values. Fig. 8 shows the FGMTO results and Table 5 summarizes the respective compliances and peak stresses. The percentage δ summarizes how less stressed FGMTO designs are compared to SMTO and MMTO designs. Relevant stress mitigation is attained on account of approaching

a fully stressed design, see the stress maps in Fig. 8. Every FGMTO result here, in terms of compliance, touches bound C^*. In fact, to reduce stresses, the more compliant the better. Ultimately, the trivial optimal solution would be structure absence.

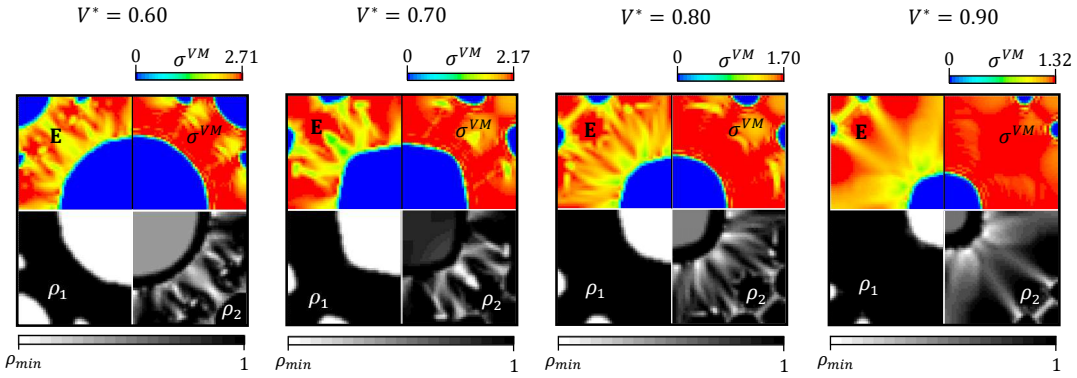

Fig. 8 Optimal designs obtained for the stress-based FGMTO problem considering different material volume fractions

Table 5 Compliance [J] and stress [MPa] results for the stress-based FGMTO problem considering different material volume fractions

		V^*			
		0.60	0.70	0.80	0.90
FGMTO	C	2986	2267	1735	1323
	$\sigma_{\max}^{\mathrm{VM}}$	2.71	2.17	1.70	1.32
δ (%)	SMTO	**- 23.8**	**- 26.4**	**- 32.0**	**- 36.8**
	MMTO	**- 12.0**	**- 10.0**	**- 15.4**	**- 10.8**

4.2. Mixed loading cases

Consider now the mixed loading cases in (31) and (32). For demonstration purposes, the SMTO problems are here solved for a specified volume fraction, $V^* = 0.80$.

4.2.1. Compliance and stress-based SMTO

The SMTO results serve as reference in the subsequent Sections for comparative purposes. In fact, benchmarks for the single-material UC subjected to the generalized average stress case are not so common in the literature, unlike the bulk and shear-type load cases. Firstly, one minimizes compliance subjected to constraint on mass (or volume, equivalently). The optimal compliance value found is then defined as the upper bound on compliance to minimize the maximal von Mises stress. The same design is found with both compliance and stress-based formulations, i.e., the stiffest and strongest designs coincide here. Fig. 9 shows the optimal layouts, a kind of an inclined ellipse is obtained when different normal stresses of same sign dominate (31) and a kind of

perforated plate exhibiting distorted rectangular holes is obtained when such remote applied stresses have opposite signs (32), shear dominated load. The respective stress plots are provided.

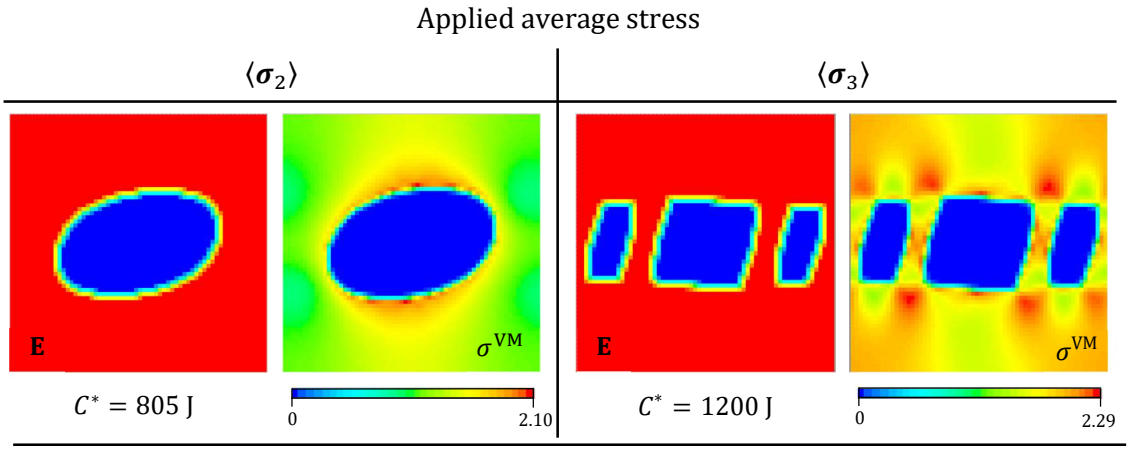

Fig. 9 SMTO results for both compliance and stress [MPa] minimization considering two average stress fields and $V^* = 0.80$

4.2.2. Stress-based MMTO

The approach here is similar to Section 4.1.2. One selects the case $V^* = 0.80$ with $m^* = 0.734$, which enforces presence of solid $\mathbf{E}_2$ (at least 10%), and compliance is worsened in approximately 25% comparing to the SMTO counterpart. The values of ζ_1 and ζ_2 for both load cases are presented in Table 6. Fig. 10 shows the layouts obtained which resemble those in Fig. 9 apart from the emerging small areas of solid $\mathbf{E}_2$. We realize that the softer phase around the hole now can lower the initial peak stress located at the hole border, on account of increasing the stresses located in inner subregions such that new stress peaks appear of lower magnitude. Table 6 also compares the compliance and peak stress between the SMTO and MMTO designs. The percentage δ shows a relevant peak stress decrease for the load $\langle \boldsymbol{\sigma}_2 \rangle$, 21.9%, but not that much for $\langle \boldsymbol{\sigma}_3 \rangle$, only 6.6%. This is consistent with the prior observations of the authors in Coelho et al. (2021), i.e., the multi-material potential for stress reduction is seen more on the side of bulk-type loads rather than shear dominated loads.

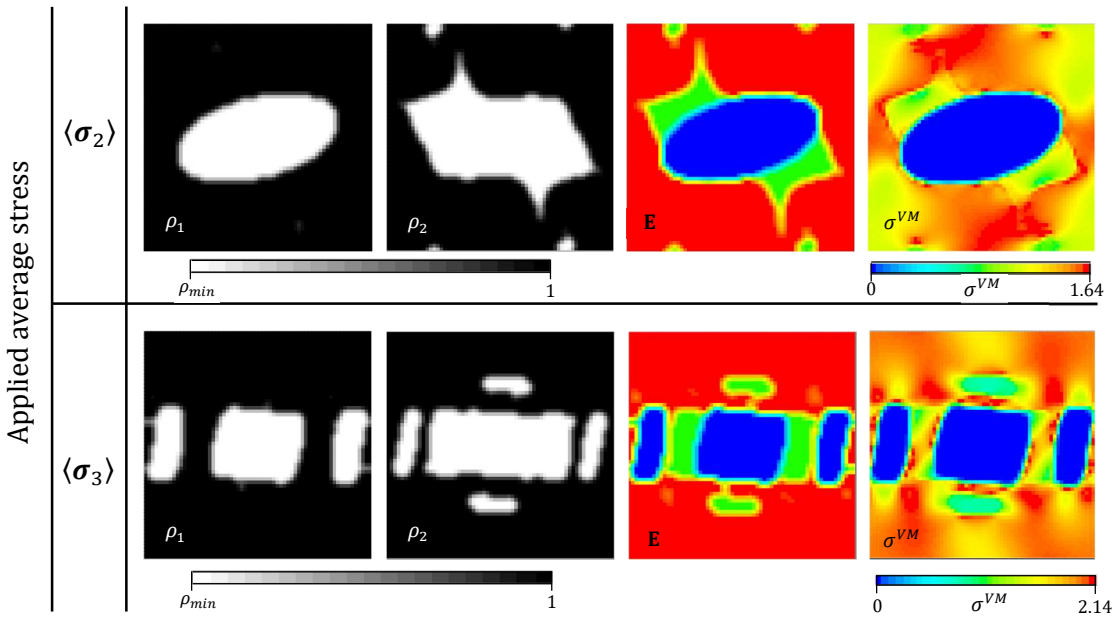

Fig. 10 Stress-based MMTO results considering two average stress fields, $V^* = 0.80$ and $m^* = 0.734$

Table 6 Results of compliance and peak stress for stress-based MMTO compared to SMTO. Values of parameters ζ_1 and ζ_2 used in MMTO

		Applied average stress	
		$\langle\sigma_2\rangle$	$\langle\sigma_3\rangle$
SMTO	C	805	1200
	$\sigma_{\max}^{\mathrm{VM}}$	2.10	2.29
MMTO	C	990	1521
	$\sigma_{\max}^{\mathrm{VM}}$	1.64	2.14
	ζ_1	23	41
	ζ_2	40	54
δ_σ (%)		**- 21.9**	**- 6.6**

4.2.3. Stress-based FGMTO

The approach here is similar to Section 4.1.3, the compliance is worsened in approximately 40% comparing to the SMTO counterpart. Fig. 11 shows the layouts obtained which now differ more from Figs. 9 and 10, as more design freedom is allowed. Table 7 summarizes the compliance and peak stress obtained with FGMTO in both load cases, and values of ζ_1 are also provided. The percentage δ shows a relevant peak stress decrease for load $\langle\boldsymbol{\sigma}_2\rangle$ when compared to the SMTO case. Stress improvements are much lower, and similar for both loads, when results are compared to MMTO. Yet, FGM overall results clearly show, in both load types, an interesting stress

mitigation effect as one approaches a fully stressed design (see the stress plots in Fig. 11), though a less remarkable stress decrease is again seen in shear dominated loads.

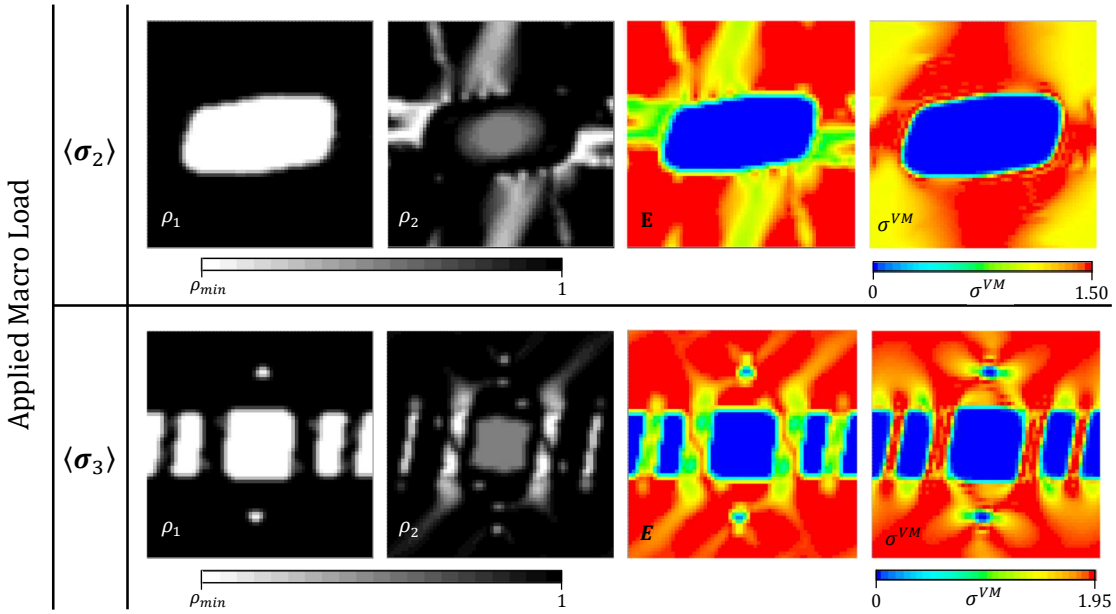

Fig. 11 Stress-based FGMTO results considering two average stress fields, $V^* = 0.80$

Table 7 Results of compliance and peak stress values for stress-based FGMTO compared to SMTO and MMTO. The values of parameter ζ_1 used in FGMTO

		Applied Macro Load	
		$\langle\sigma_2\rangle$	$\langle\sigma_3\rangle$
FGMTO	C	1127	1704
	$\sigma_{\max}^{\mathrm{VM}}$	1.50	1.95
	ζ_1	25	54
δ_σ (%)	SMTO	**- 28.6**	**- 14.9**
	MMTO	**- 8.5**	**- 8.9**

5. Conclusions

Topology optimization with stress constraints is currently a quite active research topic as it brings to the conceptual design stage an important design criterion in engineering practice that is the admissible stress. The anticipation of stress influence at earlier design stages helps attaining more efficient feasible designs at the end stage of product development. Acknowledging that, this work is a contribution to the state-of-the-art in strength-oriented microstructural TO. The minimization of maximal von Mises stress, not well covered in the literature, is explored and

extended to the multi-material setting (MMTO) to find the benefits in stress mitigation considering different types of loads, which is the main contribution here.

Two different MMTO formulations are addressed, compliance and stress-based. Firstly, the compliance-based MMTO problem is solved for a bulk-type load to find a stiffer design comparing to SMTO for the same mass requirement. Solving such problem, one shows that multi-material designs can outperform single material ones regarding stiffness, and it also impacts favourably on stress distributions. That is observed in connection with an increase in the total material volume fraction. Therefore, in applications where porosity is not mandatory, material combinations can outperform hole openings. Secondly, the stress-based problem is explored in two different ways. On one hand, one optimizes the distribution of three discrete phases, two solids plus void, which results in a conventional composite material. On the other hand, one optimizes the variation (gradation) of material properties across the UC continuous domain on account of two solids mixture amidst void, which results in an advanced composite known as FGM. The stress-based MMTO for the bulk load, renders stronger and lighter designs than SMTO while keeping the same total material volume fraction and letting the compliance be worsened. This happens on account of allowing the selection of an extra more compliant solid phase. Eventually, for no upper limit on compliance, the best for stress minimization would mean either uniform distribution of density (likely an intermediate value to comply with the volume requirement), in case no void (or hole) is enforced, or structure absence, in case porosity is enforced on design. These trivial solutions are thus skipped here as one always limit compliance enough. Also notice that under the same mass and compliance requirements, the stress-based MMTO just replicate the compliance-based MMTO optimal designs. Furthermore, fully stressed designs are here well approximated through FGMTO, which results in quite low stress levels. The corresponding designs reveal ideal solid mixtures in the continuum setting for a specific total material volume fraction. The compliance upper bound used in FGMTO is further increased, comparing to MMTO, such that enough freedom is given to the gradation of properties resulting in greater stress mitigation benefits.

The study is also extended here to other average stress fields to gain insight on how multi-material plays an important role in stress mitigation as one moves farther away from the well-studied bulk-type load. Two fields are considered, one more bulk dominated and another more shear dominated. The multi-material design advantage in lowering stresses is recognized in both cases but, as one moves toward loads where shear dominates, lesser benefits can be found. This observation gives valuable insight on the multiscale problem where material and structure are concurrently optimized. In that more complex framework, a variety of stress fields exist, spanning loads from bulk to shear type, which, as envisaged here, will impact differently in material combinations for stress mitigation. Since multiscale TO is nowadays quite a hot research topic (Wu et al. 2021), it would be an interesting research avenue bringing stress control into such problem (see e.g., Zhao et al. 2021a, 2021b), which would also advance the authors' previous works (Coelho et al. 2008; Rodrigues et al. 2002). The connectivity issue of microstructures in the multiscale problem would be also an interesting aspect to consider (see e.g., Du et al. 2018).

Finally, another relevant contribution of the present work is the parallelization of two important bottlenecks, i.e., the sensitivity analysis and the MMA optimizer. As regards the first one, important speedups are attained as presented in the Appendix. As regards MMA, an existing MPI-based parallel framework from Aage and Lazarov (2013) is quite relevant to attain important speedups when dealing with huge number of design variables. However, in the present work, the authors' greatest concern is having MMA dealing well with thousands of constraints. That is why the authors have here decided revisiting the original MMA Fortran code (Svanberg 1987) and focusing on the dual problem parallelization resorting to intel® oneAPI Math Kernel Library as

well as explicit OpenMP instructions. This is detailed in the Appendix hoping that the optimization community can easily take advantage of a few extra lines of code in original MMA to speedup computations when, in general, many problem constraints need to be considered.

The density-based MMTO methodology proposed here has its own pros and cons. Whereas it offers a well-known design freedom to efficiently capture disruptive optimal layouts, it lacks on rendering well-defined solid boundary contours. Density filtering blurs discrete phase transitions (interfaces are "gray") which raises some issues that are in the present work properly handled to accommodate discrete phase selection. However, it would be interesting to see other TO methods being applied to the same problem (e.g., the Level-set method, Wang et al. 2003), which possibly could better handle this kind of multi-phase modelling issues.

Appendix: Parallel MMA

This appendix gives an in-depth look at the MMA parallel-code implementation. Speedup curves obtained for the sensitivity analysis and a specific MMA subroutine are also shown. The FGMTO problem with $V^* = 0.90$ under bulk load, presented in Section 4.1.3, is selected here to demonstrate the efficiency of the parallel code. The hardware used by the authors is a Workstation HP Z8 G4, 2 CPUs Intel Xeon 6242R 3.1GHz 2933MHz 20C, 256GB RAM. This workstation allows us to use up to 40 physical CPU cores (plus 40 logical cores with hyperthreading). Furthermore, one uses Intel® software for programming, OneAPI Base and HPC Toolkits.

From Fig. 12a, one concludes that when optimization runs in serial mode two main bottlenecks appear: sensitivity analysis (first iterations) and MMA. Notice that only selected iterations are shown which suffices for comprehension. At each iteration one evaluates the percentage of time spent in different program routines.

The MMA solves approximate subproblems iteratively, it uses both the steepest ascent and Newton's methods to solve the dual problem, which can be a time-consuming task if several constraints are handled. Parts of the MMA code related to the dual problem are parallelized here (fine-grained parallelism). A typical MPI parallelization would involve a lot of communications that are avoided here resorting to OpenMP. Table 8 summarizes the required modifications in the original MMA FORTRAN source files (and respective subroutines): maxim.f (`HESSI` and `SUBSPA`) and maxsu.f (`XYZLAM`, `GRADI` and `LINDER`). See that the date indicated in Table 8 for these sources correspond to the MMA version accessed by the authors. Before compiling the modified code, enable the compiler to use the OpenMP directives as well as the Intel Math Kernel Library (check the actual FORTRAN project properties).

Speedup curves for the sensitivity analysis and the Hessian matrix construction (`HESSI` subroutine in MMA) are plotted in Fig. 12b. Remind that the speedup S_n is defined by

$$S_n = \frac{T_s}{T_n} \tag{33}$$

where T_s is the execution time of the serial algorithm and T_n is the execution time of the parallel algorithm with n cores. The Hessian matrix dimension β considered here to generate the `HESSI` speedup curve shown is fixed, $\beta = 2316$. This curve initially exhibits a plateau since parallelization is skipped for `NPROC`≤ 2, see Table 8. The reason is that the needed command for parallelization `!$OMP ATOMIC` has a time cost such that only when the number of processors is above 2 it becomes worthy.

One also parallelizes the MMA subroutines `XYZLAM`, `GRADI` and `LINDER`, to reduce the computational time even further since these subroutines are called quite often. From the authors'

experience, while running the examples of this work, the number of processors used in these subroutines giving a meaningful speedup is up to 8, the user-specified number indicated in Table 8.

The factorization of the Hessian matrix and the solution of the system of equations is now efficiently carried out at once by the oneMKL driver routine, `DPPSV`, instead of the original `LDLFAC` and `LDLSOL` subroutines. For instance, the authors notice that the original computational time spent in these computations is reduced at least by 99%. The subroutine `DPPSV` is suitable to solve large-scale system of equations and it also supports parallel computing.

In the present framework, the parallelization of the Hessian matrix construction and the replacement of the `LDLFAC` and `LDLSOL` subroutines by the `DPPSV` subroutine are indeed the two main factors which greatly impact on the MMA speedup.

Finally, a runtime comparison between serial and parallel codes for the entire design optimization history is shown in Fig. 12c. The proposed parallel code can reduce 82% of the total optimization runtime compared to the serial run.

Table 8 Modifications for MMA parallelization to be inserted at the indicated lines of the original MMA code.

Source	Lines	Modifications	Lines	Modifications
maxim.f (*Oct. 1999*)	95	*add* USE OMP_LIB	265	*add* USE OMP_LIB

	176	*add* NYDIM *as an argument*	302	*add the code below*
				MAXPROC = OMP_get_max_threads()
				IBETA=100
				IF (NYDIM.LE.IBETA) THEN
				NPROC=1
				ELSE
				NPROC=MAXPROC !User specified
				ENDIF
				IF (NPROC.LE.2) THEN

	211	*delete* CALL LDLFAC		
	220	*delete* CALL LDLSOL		

	221	*add the code below*
		MAXPROC = OMP_get_max_threads()
		IBETA=1000
		IF (NYDIM.LE.IBETA) THEN
		NPROC=1
		ELSE
		NPROC=MAXPROC !User specified
		ENDIF
		CALL mkl_set_num_threads(NPROC)
		CALL DPPSV('Lower', NYDIM, 1, HESSF, UU, NYDIM, INFO)
			345	*add the code below*
				ELSE
				!$OMP PARALLEL DO PRIVATE (PJ, QJ, MJ1, PIJ, QIJ, SRPJ, SRQJ, XJ,UJXJ, XJLJ, UJXJ2, XJLJ2, RR, KK, PKJ, QKJ, TTK, IK, TTI), NUM_THREADS(NPROC)
				Repeat lines 303-339 updating statement labels
				!$OMP ATOMIC
				Repeat lines 340-344 updating statement labels
				!$OMP END PARALLEL DO
				ENDIF

	222-224	*delete the lines below* DO 80 I=1,M UU(I)=DSRCH(I) 80 CONTINUE		
	255	*add* NYDIM *as an argument*		
maxsu.f (*Oct. 1999*)	19	*add the code below* NPROC=8 !User-specified !$OMP PARALLEL DO PRIVATE (PJ, QJ, MJ1, PIJ, QIJ, SRPJ, SRQJ, XJ), NUM_THREADS(NPROC)	94	*add the code below* !$OMP END PARALLEL DO
	40	*add the code below* !$OMP END PARALLEL DO	133	*add the code below* NPROC=8 !User-specified !$OMP PARALLEL DO PRIVATE (MJ1, UJXJ, XJLJ, PIJ, QIJ), NUM_THREADS (NPROC)
	82	*add the code below* NPROC=8 !User-specified !$OMP PARALLEL DO PRIVATE (MJ1, UJXJ, XJLJ, PIJ, QIJ), NUM_THREADS (NPROC)	134-144	*Replace the original code by:* DO 30 I=1,M IF(IYFREE(I).EQ.0) GOTO 30 DO 40 J=1,N MJ1=M*(J-1) UJXJ=XUPP(J)-X(J) XJLJ=X(J)-XLOW(J) PIJ=P(MJ1+I) QIJ=Q(MJ1+I) UU(I)=UU(I)+PIJ/UJXJ+QIJ/XJLJ 40 CONTINUE 30 CONTINUE
	83-93	*Replace the original code by:* DO 20 I=1,M DO 30 J=1,N MJ1=M*(J-1) UJXJ=XUPP(J)-X(J) XJLJ=X(J)-XLOW(J) PIJ=P(MJ1+I) QIJ=Q(MJ1+I) GRADF(I) = GRADF(I) + PIJ / UJXJ + QIJ / XJLJ 30 CONTINUE 20 CONTINUE	145	*add the code below* !$OMP END PARALLEL DO

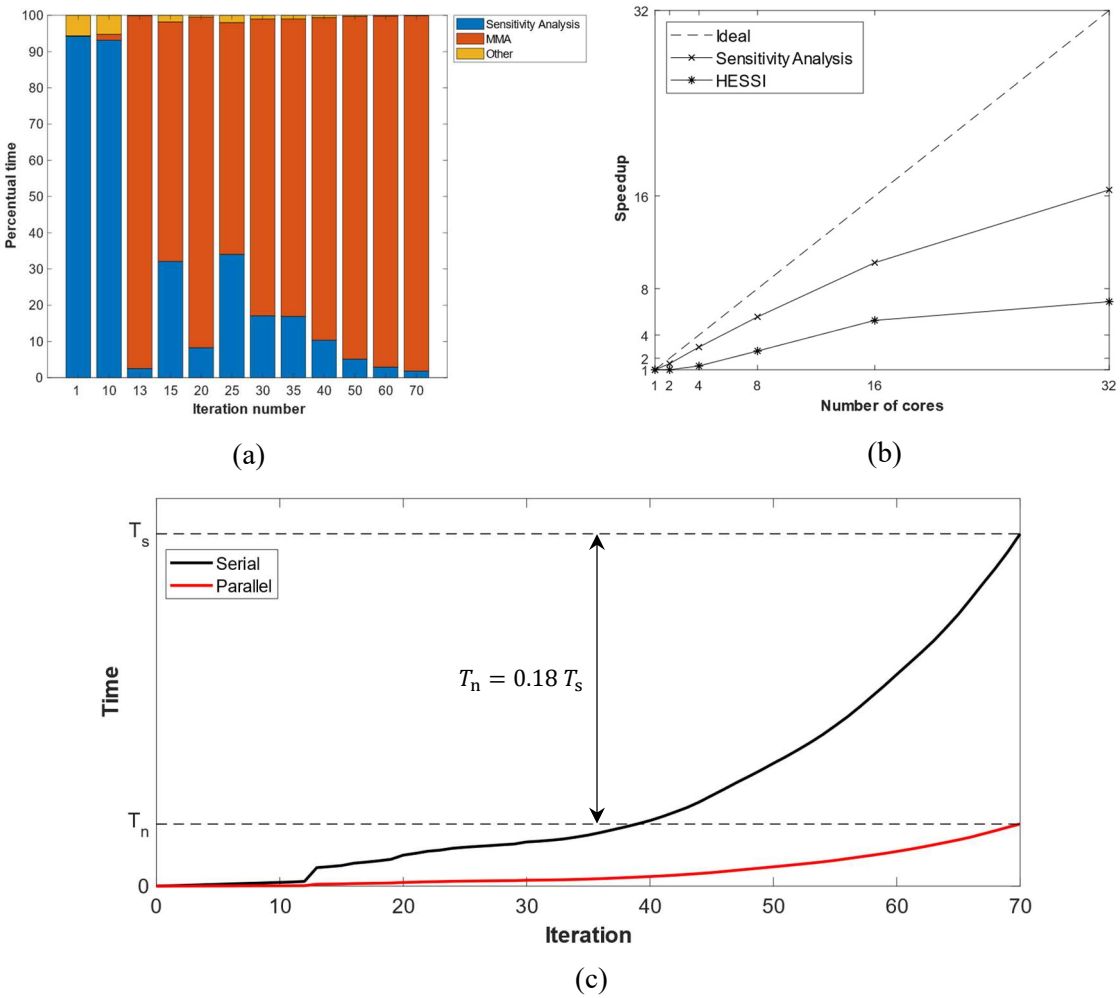

Fig. 12 Performance study of the FGMTO problem with $V^* = 0.90$ considering an applied bulk load: (a) bottlenecks identification throughout the optimization process; (b) speedup curves of the sensitivity analysis and Hessian matrix construction; (c) a comparison between serial and parallel runtimes (cumulative).

Conflict of interest

On behalf of all authors, the corresponding author states that there is no conflict of interest.

Replication of Results

This manuscript provides enough details to replicate the obtained results. Equations are presented in such way that readers can implement or solve them. The authors also use implementations that are already available in the literature as the homogenization and MMA codes. The original MMA code, that Professor Krister Svanberg kindly provides to the entire scientific community, is here parallelized. A detailed explanation on how to implement this parallel version of MMA is given, inclusive all the required code modifications (see Appendix, Table 8).

References

Aage N, Lazarov B (2013) Parallel framework for topology optimization using the method of moving asymptotes. Struct Multidisc Optim 47(4): 493-505. https://doi.org/10.1007/s00158-012-0869-2

Alacoque L, Watkins RT, Tamijani AY (2021) Stress-based and robust topology optimization for thermoelastic multi-material periodic microstructures. Comput Methods Appl Mech Eng 379: 113749. https://doi.org/10.1016/j.cma.2021.113749

Ashby M (1999) Materials selection in mechanical design (2nd Edition). Butterworth Heinemann.

Bendsøe MP (1989) Optimal shape design as a material distribution problem. Struct optim 1(4): 193-202. https://doi.org/10.1007/BF01650949

Bendsøe MP, Kikuchi N (1988) Generating optimal topologies in structural design using a homogenization method. Comput Methods Appl Mech Eng 71: 197–224. https://doi.org/10.1016/0045- 7825(88)90086-2

Bendsøe MP, Sigmund O (1999) Material interpolation schemes in topology optimization. Arch Appl Mech 69: 635-654. https://doi.org/10.1007/s004190050248

Bendsøe M, Sigmund O (2004) Topology optimization: theory, methods and applications. Springer-Verlag, Berlin. https://doi.org/ 10.1007/978-3-662-05086-6

Bourdin B, Chambolle A (2003) Design-dependent loads in topology optimization. ESAIM – Control Optim Calc Var 9: 19–48. https://doi.org/10.1051/cocv:2002070

Bruggi M (2008) On an alternative approach to stress constraints relaxation in topology optimization. Struct Multidisc Optim 36(2): 125-141. https://doi.org/10.1007/s00158-007-0203-6

Bruggi M, Duysinx P (2012) Topology optimization for minimum weight with compliance and stress constraints. Struct Multidisc Optim 46: 369–384. https://doi.org/10.1007/s00158-012-0759-7

Bruns T, Tortorelli D. (2001) Topology optimization of non-linear elastic structures and compliant mechanisms. Comput Methods Appl Mech Eng 190(26-27): 3443-3459. https://doi.org/10.1016/S0045-7825(00)00278-4

Bruyneel M (2011) SFP - a new parameterization based on shape functions for optimal material selection: application to conventional composite plies. Struct Multidisc Optim 43(6): 17-27. https://doi.org/10.1007/s00158-010-0548-0

Cherepanov GP (1974) Inverse problems of the plane theory of elasticity. J Appl Math Mech 38: 915-931. https://doi.org/10.1016/0021-8928(75)90085-4

Coelho PG, Barroca BC, Conde FM, Guedes JM (2021) Minimization of maximal von Mises stress in porous composite microstructures using shape and topology optimization. Struct Multidisc Optim 64: 1781-1799. https://doi.org/10.1007/s00158-021-02942-y

Coelho PG, Fernandes PR, Guedes JM, Rodrigues HC (2008) A hierarchical model for concurrent material and topology optimization of three-dimensional structures. Struct Multidisc Optim, 35(2): 107-115. https://doi.org/10.1007/s00158-007-0141-3

Coelho PG, Guedes JM, Cardoso JB (2019) Topology optimization of cellular materials with periodic microstructure under stress constraints. Struct Multidisc Optim 59(2): 633-645. https://doi.org/10.1007/s00158-018-2089-x

Collet M, Noël L, Bruggi M, Duysinx P (2018) Topology optimization for microstructural design under stress constraints. Struct Multidisc Optim 58(6): 2677-2695. https://doi.org/10.1007/s00158-018-2045-9

Conlan-Smith C, James KA (2019) A stress-based topology optimization method for heterogeneous structures. Struct Multidisc Optim 60: 167–183. https://doi.org/10.1007/s00158-019-02207-9

da Silva GA, Aage N, Beck AT, Sigmund O (2020) Three-dimensional manufacturing tolerant topology optimization with hundreds of millions of local stress constraints. Int J Numer Methods Eng 122(2): 548–578. https://doi.org/10.1002/nme.6548

da Silva GA, Aage N, Beck AT Sigmund O (2021) Local versus global stress constraint strategies in topology optimization: A comparative study. Int J Numer Methods Eng 122(21): 6003 – 6036. https://doi.org/10.1002/nme.6781

Dagum L, Menon R (1998) OpenMP: an industry standard API for shared-memory programming. IEEE computational science and engineering, 5(1), 46-55. https://doi.org/10.1109/99.660313

Deaton JD, Grandhi RV (2014) A survey of structural and multidisciplinary continuum topology optimization: post 2000. Struct Multidiscip Optim 49:1–38. https://doi.org/10.1007/s00158-013-0956-z

Du Z, Zhou XY, Picelli R, Kim HA (2018) Connecting microstructures for multiscale topology optimization with connectivity index constraints. J Mech Des 10(1115/1):4041176. https://doi.org/10.1115/1.4041176

Duysinx P, Bendsøe M (1998) Topology optimization of continuum structures with local stress constraints. Int J Numer Methods Eng 43(8): 1453-1478. https://doi.org/10.1002/(SICI)1097-0207(19981230)43:8<1453::AID-NME480>3.0.CO;2-2

Giraldo-Londoño O, Aguiló MA, Paulino GH (2021) Local stress constraints in topology optimization of structures subjected to arbitrary dynamic loads: a stress aggregation-free approach. Struct Multidiscip Optim 64: 3287–3309. https://doi.org/10.1007/s00158-021-02954-8

Giraldo-Londoño O, Paulino GH (2021) PolyStress: a Matlab implementation for local stress-constrained topology optimization using the augmented Lagrangian method. Struct Multidiscip Optim 63: 2065–2097. https://doi.org/10.1007/s00158-020-02760-8

Guedes J, Kikuchi N (1990) Pre-processing and postprocessing for materials based on the homogenization method with adaptive finite element methods. Comput Methods Appl Mech Eng 83(2): 143-198. https://doi.org/10.1016/0045-7825(90)90148-F

Gropp W, Lusk E, Skjellum A (1999) Using MPI: portable parallel programming with the message passing interface. Second Edition. MIT Press

Guo X, Zhang W, Zhong W (2014) Stress-related topology optimization of continuum structures involving multi-phase materials. Comput Methods Appl Mech Eng 268: 632-655. https://doi.org/10.1016/j.cma.2013.10.003

Hashin Z, Shtrikman S (1963) A variational approach to the theory of the elastic behaviour of multiphase materials. J Mech Phys Solids 11(2): 127-140. https://doi.org/10.1016/0022-5096(63)90060-7

Haug EJ, Choi KK, Komkov V (1986) Design sensitivity analysis of structural systems. Academic Press Inc., Orlando

Hvejsel CF, Lund E (2011) Material interpolation schemes for unified topology and multi-material optimization. Struct Multidisc Optim 43(6): 811-825. https://doi.org/10.1007/s00158-011-0625-z

Hvejsel C F, Lund E, Stolpe M (2011) Optimization strategies for discrete multi-material stiffness optimization. Struct Multidisc Optim 44(2): 149-163. https://doi.org/10.1007/s00158-011-0648-5

Ituarte IF, Boddeti N, Hassani V, Dunn ML, Rosen DW (2019) Design and additive manufacture of functionally graded structures based on digital materials. Addit Manuf 30: 100839. https://doi.org/10.1016/j.addma.2019.100839

James KA (2018) Multiphase topology design with optimal material selection using an inverse p-norm function. Int J Numer Methods Eng 114(9): 999-1017. https://doi.org/10.1002/nme.5774

Jung Y, Lim S, Kim J, Min S (2020) Lightweight design of electric bus roof structure using multi-material topology optimisation. Struct Multidisc Optim 61(3): 1273-1285. https://doi.org/10.1007/s00158-019-02410-8

Kennedy GJ (2016) A full-space barrier method for stress-constrained discrete material design optimization. Struct Multidisc Optim 54(3): 619-639. https://doi.org/10.1007/s00158-016-1428-z

Kennedy GJ, Chin TW (2019) A sequential convex optimization method for multimaterial compliance design problems. Comput Struct 212: 110-124. https://doi.org/10.1016/j.compstruc.2018.10.007

Li C, Kim IY (2018) Multi-material topology optimization for automotive design problems. Proc Institut Mech Eng Part D: J Autom Eng 232: 1950–1969. https://doi.org/10.1177/0954407017737901

Li D, Kim IY (2018) Multi-material topology optimization for practical lightweight design. Struct Multidisc Optim 58(3), 1081-1094. https://doi.org/10.1007/s00158-018-1953-z

Liu J, Gaynor AT, Chen S et al. (2018) Current and future trends in topology optimization for additive manufacturing. Struct Multidisc Optim 57: 2457–2483. https://doi.org/10.1007/s00158-018-1994-3

Long K, Wang X, Gu X (2018) Local optimum in multi-material topology optimization and solution by reciprocal variables. Struct Multidisc Optim 57(3): 1283-1295. https://doi.org/10.1007/s00158-018-1953-z

Luenberger D, Ye Y (1984). Linear and nonlinear programming (Vol. 2). Reading, MA: Addison-wesley. https://doi.org/10.1007%2F978-3-319-18842-3

Picelli R, Townsend S, Alicia Kim H (2020) Microstructural Stress Shape Optimization Using the Level Set Method. J Mech Des 142(11): 111705. https://doi.org/10.1115/1.4047152

Noël L, Duysinx P (2017) Shape optimization of microstructural designs subject to local stress constraints within an XFEM-level set framework. Struct Multidiscip Optim 55:2323–2338. https://doi.org/10.1007/s00158-016-1642-8

Ramani A (2011) Multi-material topology optimization with strength constraints. Struct Multidisc Optim 43: 597-615. https://doi.org/10.1007/s00158-010-0581-z

Rodrigues H, Guedes JM, Bendsøe MP (2002) Hierarchical optimization of material and structure. Struct Multidisc Optim 24(1): 1-10. https://doi.org/10.1007/s00158-002-0209-z

Sanders ED, Aguiló MA, Paulino GH (2018) Multi-material continuum topology optimization with arbitrary volume and mass constraints. Comput Methods Appl Mech Eng 340: 798-823. https://doi.org/10.1016/j.cma.2018.01.032

Senhora FV, Giraldo-Londoño O, Menezes IFM. *et al.* (2020) Topology optimization with local stress constraints: a stress aggregation-free approach. Struct Multidisc Optim 62: 1639–1668. https://doi.org/10.1007/s00158-020-02573-9

Sigmund O (2007) Morphology-based black and white filters for topology optimization. Struct Multidiscip Optim 33:401–424. https://doi.org/10.1007/s00158-006-0087-x

Sigmund O, Maute K (2013) Topology optimization approaches. Struct Multidisc Optim 48, 1031–1055. https://doi.org/10.1007/s00158-013-0978-6

Sivapuram R, Picelli R, Yoon GH, Yi B (2021) On the design of multimaterial structural topologies using integer programming. Comput Methods Appl Mech Eng 384: 114000, https://doi.org/10.1016/j.cma.2021.114000

Sokolowski J, Zochowski A (1999) On the Topological Derivative in Shape Optimization. SIAM J Control Optim 37(4): 1251–1272. https://doi.org/10.1137/S0363012997323230

Stegmann J, Lund E (2005) Discrete material optimization of general composite shell structures. Int J Numer Methods Eng 62: 2009-2027. https://doi.org/10.1002/nme.1259

Svanberg K (1987) The method of moving asymptotes - a new method for structural optimization. Int J Numer Methods Eng 24:359–373. https://doi.org/10.1002/nme.1620240207

Tavakoli R, Mohseni SM (2014) Alternating active-phase algorithm for multimaterial topology optimization problems: a 115-line MATLAB implementation. Struct Multidisc Optim 49: 621-642. https://doi.org/10.1007/s00158-013-0999-1

Taylor J, Bendsøe M (1984) An interpretation of min-max structural design problems including a method for relaxing constraints. Int J Solids Struct 20: 301-314. https://doi.org/10.1016/0020 -7683(84)90041-6

Vigdergauz S (2016) A planar grained structure with a multiphase nested inclusion in a periodic cell: Elastostatic solution and the equi-stressness. Math Mech Solids 21(6):709–724. https://doi.org/10.1177/1081286514536084

Vigdergauz S (2001) The effective properties of a perforated elastic plate numerical optimization by genetic algorithm. Int J Solids Struct 38: 8593–8616. https://doi.org/10.1016/S0020-7683(01)00189-5

Vigdergauz S (2002) Genetic algorithm of the effective Young moduli in a perforated plate. Struct Multidisc Optim 24(2): 106–117. https://doi.org/10.1007/s00158-002-0221-3

Vigdergauz S (1993) Optimal stiffening of holes under equibiaxial tension. Int J Solids Struct 30(4): 569–577. https://doi.org/10.1016/0020-7683(93)90188-D

Wang MY, Wang X (2004) “Color” level sets: a multi-phase method for structural topology optimization with multiple materials. Comput Methods Appl Mech Eng 193(6-8): 469-496. https://doi.org/10.1016/j.cma.2003.10.008

Wang MY, Wang X, Guo D (2003) A level set method for structural topology optimization. Comput Methods Appl Mech Eng 192(1-2): 227-246. https://doi.org/10.1016/S0045-7825(02)00559-5

Woischwill C, Kim IY (2018) Multimaterial multijoint topology optimization. Int J Numer Methods Eng 115(13): 1552-1579. https://doi.org/10.1002/nme.5908

Wu J, Sigmund O, Groen JP (2021) Topology optimization of multi-scale structures: a review. Struc Multidisc Optim 63: 1455-1480. https://doi.org/10.1007/s00158-021-02881-8

Xia Q, Wang MY (2008) Simultaneous optimization of the material properties and the topology of functionally graded structures. Comput Aided Des 40: 660-67. https://doi.org/10.1016/j.cad.2008.01.014

Yin L, Ananthasuresh GK (2001) Topology optimization of compliant mechanisms with multiple materials using a peak function material interpolation scheme. Struc Multidisc Optim 23: 49-62. https://doi.org/10.1007/s00158-001-0165-z

Zhao L, Xu B, Han Y, Rong J (2021a) Concurrent design of composite macrostructure and cellular microstructure with respect to dynamic stress response under random excitations. Compos Struct 257: 113123. https://doi.org/10.1016/j.compstruct.2020.113123

Zhao R, Zhao J, Wang C (2021b) Stress-constrained concurrent topology optimization of two-scale hierarchical structures. Int J Numer Methods Eng 122(21): 6126-6154. https://doi.org/10.1002/nme.6785

Zhou S, Wang MY (2007) Multimaterial structural topology optimization with a generalized Cahn–Hilliard model of multiphase transition. Struct Multidisc Optim 33: 89-111. https://doi.org/10.1007/s00158-006-0035-9

Zuo W, Saitou K (2017) Multi-material topology optimization using ordered SIMP interpolation. Struct Multidisc Optim 55: 477-491. https://doi.org/10.1007/s00158-016-1513-3